Journal of Applied Fluid Mechanics, Vol. 19, No. 1, pp. 3149-3169, 2026. Available online at www.jafmonline.net, ISSN 1735-3572, EISSN 1735-3645. https://doi.org/10.47176/jafm.19.1.3680



Multi-objective Optimization of Horizontal Axis Wind Turbine Arrays: **Impact of Spacing Distance on Noise Generation and Power Efficiency**

A. Amoura¹, S. Khelladi², A. Smaili¹, M. N. Hamlaoui^{1†}, and S. Kouidri²

¹ Laboratory of Green and Mechanical Development (LGMD), Ecole Nationale Polytechnique -ENP. P.B. 182 EL Harrach, Algiers, 16200, Algeria

² Arts et Métiers Institute of Technology, CNAM, LIFSE, F-75013, Paris, France

†Corresponding Author Email: mohammed nadjib.hamlaoui@g.enp.edu.dz

ABSTRACT

This work explores the effect of spacing between co-axially positioned Horizontal Axis Wind Turbines (HAWTs) on their aerodynamic behavior and acoustic emissions under uniform inflow conditions. The aerodynamic simulations employ the Actuator Disk Method (ADM) integrated within an Unsteady Reynolds-Averaged Navier-Stokes (URANS) framework, utilizing the standard k-E turbulence model to resolve near-wake turbulent structures. For noise prediction, the Ffowcs Williams-Hawkings (FW-H) acoustic analogy is applied using the Farassat-1A formulation on a permeable spherical surface surrounding the rotor to estimate the generated acoustic pressures. These pressure signals served as input sources for far-field noise computations based on the Linearized Euler Equations (LEE). The findings demonstrate that wake interactions significantly influence the downstream turbine's performance and acoustic output in multiple-turbine arrangements. A multi-objective optimization process was carried out to achieve a trade-off between energy production and acoustic emissions, identifying an inter-turbine spacing of 6D as an optimal configuration. The study also emphasizes the limitations of relying solely on single-turbine aeroacoustic models for wind farm analysis, underscoring the necessity of full-scale aeroacoustic evaluation when considering wake effects and acoustic interference among turbines.

Article History

Received May 15, 2025 Revised August 11, 2025 Accepted August 15, 2025 Available online November 5, 2025

Keywords:

Aeroacoustics Actuator disk Linearized Euler equations Ffowcs Williams and Hawkings Acoustic analogies Wind turbine noise

INTRODUCTION

The growing interest in clean energy has led to a rapid deployment of wind farms, driven by the pressing need to mitigate climate change and reduce reliance on fossil fuels. According to the Global Wind Energy Council (2024), 2023 was a historic year for wind installation, where the global wind energy sector achieved a remarkable installation record, with 117 GW of new capacity added worldwide. This represents a 50% increase compared to 2022, highlighting significant growth across continents, driven predominantly by China, which accounted for 75 GW (i.e., approximately 65% of the global additions). However, as wind farms increase, so do concerns about the noise they produce. The distinctive tonal and varying characteristics of wind turbine noise have heightened community concerns, distinguishing it from other environmental noise sources and bringing attention to the importance of understanding and managing its impact on nearby residents. Wind farm noise

remains a controversial subject, and its complexity increases when coupled with the objective of optimizing energy production in these installations (Shen et al., 2019). According to the International Standard ISO-1996-1 (2016), noise levels in residential areas remain between 35 and 45 dB(A), with higher limits of around 50 dB(A) considered acceptable in industrial zones. These guidelines are adaptable, allowing for adjustments to align with local regulatory standards where applicable.

In wind farm design, optimizing turbine layout is critical, as the arrangement and spacing of turbines significantly influence power output, overall annual energy production, and noise emissions. Turbine spacing plays a pivotal role in managing wake effects that impact downstream turbine performance and in controlling noise emissions that affect surrounding communities. Achieving an optimal layout requires balancing these competing factors to enhance energy efficiency while maintaining environmental compatibility. Much of the existing research materials primarily focuses on the aerodynamic aspects of wind turbines, including detailed studies on airfoil behavior, aerodynamic forces acting on turbine blades, and the design of rotor blades for improved efficiency (Hamlaoui et al., 2024a & b), while numerous studies have also studied the wake interactions within wind farms to optimize turbine positioning and performance from an aerodynamic perspective (Zergane et al., 2018; Grady et al., 2005; Mittal, 2010 & Rahmani et al., 2010).

In contrast, the acoustic implications, particularly wake-induced noise interactions between turbines, have received less attention. Few studies have adequately addressed these acoustic aspects, despite the importance of noise generation in these configurations. Multiobjective optimization studies that consider both energy output and noise generation often rely on simplified models for practical assessments. These models typically combine aerodynamic wake models with sound propagation models, such as the widely used ISO 9613-2 (1996) standard, which provides an engineering framework for estimating sound attenuation during outdoor propagation. For instance, Kwong et al. (2012) and Sorkhabi et al. (2016) employ different version of genetic algorithms to investigate the trade-off between energy output and noise reduction under various constraints. In contrast to earlier works that assumed identical noise sources, later research integrated more detailed noise generation models, such as Hubbard and BPM, while some adopted advanced propagation approaches like the Parabolic Equation (PE) model to account for atmospheric and terrain effects beyond ISO's capabilities (Tingey & Ning, 2017; Cao et al., 2020; Nyborg et al., 2023).

These study shows how various aerodynamic and acoustic models significantly influence the accuracy of wind farms layout optimization. Achieving precise assessments and predictions of HAWT aerodynamic noise is crucial aspects before any installation, yet estimating such flow-induced noise remains a fundamental challenge, particularly due to the substantial disparities in length and time scales inherent in the unsteady aerodynamic flow field and the unsteady acoustic radiation field in aeroacoustics simulations (Wang et al., 2007). Simulating such complex flows around wind turbines requires advanced numerical methods. However, due to the high computational costs associated with the direct simulations and the large eddy simulations (LES) of the full rotor, relying on these methods is typically impractical, especially for large scale simulation, despite their acknowledged accuracy. Therefore, HAWT aerodynamic analysis are often carried out through three primary models. This includes the standard actuator disk (AD-std) model, a combination of the blade element and the actuator disk concept known as the actuator disk model (ADM), lastly, the actuator line model (ALM), which parametrizes the rotor-induced forces as line elements distributed along each blade (Lin & Porté-Agel, 2022).

In this context, the work of Lin and Porté-Agel (2022) investigated the application of LES to predict flow patterns in wind turbine arrays under active yaw control. Their findings demonstrated that the ADM strikes an

effective balance between computational efficiency and precision, making it well-suited for simulating wind farm flows under various conditions, such as partial wake and active yaw control. Hamlaoui et al., (2021a; 2022) proposed refined corrections for the stall delay effects to better predict the performance and near-wake characteristics of small HAWT operating at low Reynolds numbers. Their approach involved the development of an in-house subroutine ADM, referred to as "AD LGMD," implemented within the OpenFOAM framework to solve the three-dimensional Navier-Stokes equations in cylindrical coordinates. The simulated results aligned well with experimental data, particularly in terms of wake structure and the nacelle's impact on flow characteristics. Subsequent refinements to the Stall Delay Approach (SDA) incorporated an empirical correlation to account for radial variations in the 3D stall angle, derived from observations of the NREL Phase VI dataset (Hamlaoui et al., 2024a).

For most HAWT, the Mach number typically remains well below the compressible threshold ($M_a < 0.3$). This characteristic allows decoupled modeling approaches, wherein the assessment of noise sources and their propagation are conducted independently. The process involves the computation of local pressure fluctuations near the blade through a flow solver confined to a limited area around the rotor. Subsequently, these data serve as input to a simplified wave propagation model, covering large regions at less expensive computational cost (Tadamasa & Zangeneh, 2011).

Kirchhoff approach or the acoustic analogies are an effectives method for predicting far-field noise propagation. However, these analytical approaches solve scalar equations at discrete locations or directions corresponding to the receivers' positions. Among them, the Ffowcs Williams-Hawkings (FW-H) acoustic analogy, which is particularly suitable for modeling noise generated by HAWT (Farassat, 2007), as it extends Lighthill's analogy by accounting for moving boundaries and incorporates three distinct acoustic sources terms, allowing for more comprehensive noise prediction from rotating blades. Additionally, this analogy offers flexibility in practical applications through porous control surfaces that allow the flow of mass, momentum, and energy across boundaries (Luo & Lai, 2006). However, its assumption of a homogeneous medium overlooks important factors such as refraction effects and the impact of mean flow on wave propagation, as its solution relies on the Green's function of the wave equation in an unbounded space. To address these limitations, the Linearized Euler Equations (LEE) provide a more robust alternative for modeling wave propagation, accounting for mean flow effect and supporting the existence of obstacle surfaces, making them a valuable tool for simulating realistic noise propagation. Their development and validation remain active areas addressed in numerous studies.

Hybrid computational methods that couple aerodynamic and acoustic solvers have become increasingly prominent in aeroacoustics research due to their ability to compromise accuracy and computational efficiency. Khelladi et al. (2011) investigated the use of

the finite volume method with a flow reconstruction via Moving Least Squares (MLS) approximation. Two distinct approaches were evaluated: an explicit time integration scheme for zero-mean reconstruction, and an implicit time integration scheme for mass-matrix formulation. The latter demonstrated fifth order accuracy in predicting wave propagation based on the LEE. Their tests demonstrated high accuracy and stability in predicting wave behavior, even with complex geometries.

Kim et al. (2015) applied Dispersion-relationpreserving finite-difference for solving the LEE, investigating airfoil geometry's effect on noise emissions when subjected to homogeneous and isotropic turbulence. Through numerical analysis of a symmetric airfoil, they derived an algebraic expression for the acoustic power spectrum, which aligned well with their numerical results. Legendre et al. (2018) adopted a hybrid approach using the Stochastic Noise Generation and Radiation (SNGR) method, which synthesizes noise sources to be applied on the right-hand side of the LEE. This method uses timeaveraged flow fields from RANS simulations to generate aeroacoustic sources, significantly reducing computational costs. Colas et al. (2023) Relied on Amiet's theory as source model for performing a comparison of two propagated method, namely: the LEE and the parabolic equation (PE), and exploring the effect of wind farm flow on wind turbine noise propagation. Their findings offer valuable insights into how different propagation methods influence noise predictions and how wind farm configurations affect noise levels perceived at distant locations. Yang et al. (2022) assessed the impact of non-uniform flow fields on the propagation of helicopter rotor noise. Using a Hybrid CAA method, the study couples Computational Fluid Dynamics (CFD) simulations with Computational Aeroacoustics (CAA) simulations using LEE. The coupling involves an acoustic source extraction technique based on pressure and pressure gradients data to transfer acoustic information from the CFD domain to the CAA solver. Robin and Legendre (2002) investigated the noise propagation from wind turbines under complex environmental conditions. The study employs the LEE solved using a high-order adaptive Discontinuous Galerkin (DG) method in the time domain. A simplified propeller noise model is used to simulate thickness and loading noise sources, by using a cloud of rotating point sources applied to the right-hand side of the mass and momentum conservation equations.

In the light of above discussion, this study adopts a novel hybrid methodology that integrates CFD and CAA to accurately predict the HAWT noise generation and propagation. Separating the aerodynamic computations from acoustic propagation analysis, allows for the use of the most appropriate modeling technique at each stage of the process. This hybrid approach has been validated in prior studies (Amoura et al., 2022 & 2025) using the NREL phase VI (National Renewable Energy Laboratory) HAWT under various operating conditions, establishing robustness and versatility. The numerical computational is established through the integration of three distinct models. First, the ADM, which integrates actuator disk concept with blade elements theory, captures the interaction between the flow and the wind turbine,

allowing precise calculations of instantaneous turbulent flow in near field. ADM is widely used in wind turbine simulations due to its ability to provide an efficient yet accurate representation of aerodynamic forces while avoiding the computational expense of full rotor resolved simulations. Second, the FW-H acoustic analogy is employed to model the primary sources of aerodynamic noise generated by the wind turbines. Unlike semiempirical models that classify noise sources into inflow turbulence noise and airfoil self-noise, the permeable FW-H formulation does not categorize sources in the same separate manner. Instead, it captures all noise contributions within the defined control surface, including monopole, dipole, and even quadrupole sources. This ensures that all relevant acoustic disturbances generated by the actuator disk, including wake-induced fluctuations, are accounted for, making the FW-H analogy a powerful tool for wind turbine noise analysis. The influence of different FW-H permeable surface shapes on acoustic predictions has been further explored in a recent study on UAV propellers, where various surface geometries were tested. Broatch et al. (2024) found that cylindrical surfaces led to higher SPL values at low frequencies due to vortical structures passing through the bottom cap, while spherical surfaces provided more consistent and reliable results. Although FW-H is commonly employed for far-field noise prediction, its assumptions of free-field propagation without interaction with environmental factors limit its applicability in realistic scenarios. So instead of directly used this analogy for acoustic prediction, the goal was to develop a method ultimately capable of performing 3D calculations while accounting for terrain topology, urban areas, interference phenomenon and mean wind flow effects. In this context, integrating the FW-H acoustic analogy as a transitional is particularly advantageous, as it addresses a key challenge in fluid-acoustic coupling by providing a practical and efficient means of modeling acoustic pressure fluctuations. These fluctuations serve as noise source terms in the LEE, which govern far-field noise propagation while accommodating complex wave interactions with mean flow effects and obstacles. By integrating these models, the proposed approach provides a novel and computationally efficient solution for wind turbine noise prediction, offering a well-balanced framework that maintains accuracy while significantly reducing computational cost.

Leveraging the proposed hybrid approach, the present study investigates the influence of separation distances between multiple HAWT on their aerodynamic performances and noise generation. The aim is to determine optimal configurations for multi-turbine layouts that maximize energy production while minimizing noise emissions. Additionally, the study assesses the relevance of modeling an entire wind farm based on a comprehensive aeroacoustics analysis of an isolated turbine, exploring how this approach can simplify modeling without compromising accuracy, especially in complex configurations where wake effects and wave interference significantly impact noise propagation.

The present paper begins by describing the various models employed in the proposed methodology (Sec. 2), followed by the numerical setup and details of the

investigation cases (Sec. 3), while Section 4 covers the simulation results and the finding from the optimization study. Finally, the conclusions are drawn in Section 5.

2 MATHEMATICAL MODEL

2.1 Aerodynamic Considerations:

The aerodynamic calculations have been carried out using the ADM under uniform flow conditions; thus, the axisymmetric formulation of the Navier-Stokes (NS) equations remains sufficient for the flow field reproduction around HAWTs rotor by assuming flow symmetry relative to the rotational axis. This assumption substantially reduces the computational resources required while still capturing key flow characteristics around the HAWT blades. The compressible axisymmetric NS equations describing the turbulent flow around HAWT have been expressed as follows:

$$\frac{\partial \rho}{\partial t} + \frac{\partial (\rho u_j)}{\partial x_i} = 0 \tag{1}$$

$$\frac{\partial (\rho u_i)}{\partial t} + \frac{\partial (\rho u_i u_j)}{\partial x_i} = -\frac{\partial p}{\partial x_i} + \frac{\partial}{\partial x_j} \left[(\mu + \mu_t) \frac{\partial u_j}{\partial x_j} \right] + \rho \, f_{BF,i} \qquad (2)$$

$$\frac{\partial(\rho h)}{\partial t} + \frac{\partial(\rho u_j h)}{\partial x_j} + \frac{\partial(\rho k)}{\partial t} + \frac{\partial(\rho u_j k)}{\partial x_j} - \frac{\partial p}{\partial t} = -\frac{\partial q_i}{\partial x_j} + \frac{\partial(u_j \tau_{ij})}{\partial x_j}$$
(3)

In the above equations, u_i represents the mean velocity, and p denotes the pressure, where μ and μ_t correspond to the dynamic and eddy viscosity, respectively. The term $f_{BF,i}$ refers to the actuator disk body force acting upon the flow field. The tensor τ_{ij} accounts for the viscous stresses, and q_j denotes the heat flux. The enthalpy h is defined as the sum of the internal energy and the pressure-density ratio, expressed as $h=e+p/\rho$, where $(e=c_vT)$ represents the internal energy. For compressible flows, the fluctuating density is extracted by linking between the momentum and energy equation throughout thermodynamic equation of state $(p=\rho RT)$.

To incorporate the effect of wind turbine blades within this framework without explicitly resolving their geometry, the actuator disk method (ADM) is introduced. In this approach, the rotor is modeled as a permeable surface over the swept area of the turbine, where a distributed body force $f_{BF,i}$ is applied directly to the momentum equations. This force represents the aerodynamic loading exerted by the blades, inducing a pressure jump across the disk and thereby modifying the surrounding flow field. Geometrically, the actuator disk is often represented as a conical surface, where the base radius is defined by $R \cos \gamma$ where R denoting the blades length and γ the conning angle, typically, ranging between 0° and 10° (Masson et al., 2001).

The actuator disk concept is often coupled to the blade element theory, which estimates the aerodynamic sectional forces exerted by the HAWT blades, assuming that the rotor has no radial effect $(dF_r = 0)$ on the flow field. Consequently, at a given radial position, the distributed surface forces associated with an infinitesimal actuator disk element could be segregated into normal and tangential (dF_z, dF_θ) components. Typical HAWT rotors

are usually characterized by rotational speed Ω , B number of blades, pitch angle θ_p and local twist and chord (β, c) varying radially from the root to the tip of the rotor blade respectively.

The aerodynamic forces exerted by the rotor, expressed per unit blade length, are derived based on the relative velocity W, defined at each radial station as the combination of the incoming axial flow and the blade's rotational motion. This relative velocity is decomposed into axial and tangential components, from which the flow angle ϕ is determined. The flow angle is then used to compute the geometric angle of attack, which in turn governs the evaluation of the lift and drag coefficients. These aerodynamic force components are subsequently projected onto the axial and tangential directions, resulting in the volume force components (f_z) and (f_θ) , which represent the rotor body forces applied to the flow field and are directly incorporated into the momentum equations.

$$f_z = \frac{dF_z}{dv} = \frac{1}{2\pi r dz} \frac{1}{2} B\rho W^2 F(C_l \cos \phi + C_d \sin \phi) c \qquad (4)$$

$$f_{\theta} = \frac{dF_{\theta}}{dv} = \frac{1}{2\pi r dz} \frac{1}{2} B\rho W^2 F(C_l \sin \phi + C_d \cos \phi) c \qquad (5)$$

To address the ADM's assumption of an infinite number of blades and to incorporate the effects of blade tip vortices, three distinct Tip Loss Correction Factors (TLCF) were considered: Glauert (1963), Shen et al. (2005), and Wimshurst and Willden (2017). These models are then compared in order to identify the appropriate predictions. It should be noted that these TLCF share common formulation with different considerations on the blade root and tip effect implication. In this context, the index k corresponds to the axial (\vec{z}) and tangential ($\vec{\theta}$) directions, respectively.

Glauert's approach incorporates both tip and hub losses $(F = F_{root}, F_{tip})$, ensuring that the influence of the blade root trailing vortices is considered alongside the loss estimation. The use of the formulation proposed by Glauert consists on setting the parameter g_k to 1 in Eq.4. Conversely, Wimshurst and Willden (2017), as well as Shen et al. (2005), focus exclusively on the tip correction factor, assuming no significant root effects, by setting a constant root correction factor to $F_{root} = 1$.

$$\begin{cases} F = F_{root} \cdot F_{tip} \\ F_{tip} = \frac{2}{\pi} cos^{-1} \left[exp \left(-g_k \frac{B(R-r)}{2r \sin \phi} \right) \right] \\ F_{root} = \frac{2}{\pi} cos^{-1} \left[exp \left(-g_k \frac{B(R-R_{hub})}{2r \sin \phi} \right) \right] \end{cases}$$
 (6)

where:
$$g_k = \exp(-a_k(B\lambda - b_\lambda)) + 0.1$$

Notably, Shen et al. (2005) propose constant values for the parameters $a_k = 0.125$ and $b_k = 21$ for the TLCF, in both axial and tangential directions, where Wimshurst and Willden (2017) consider that the loss amount is more significant in the tangential direction compared to the axial one. Thus, their model adjusts distinct constants depending on the assumed direction ($a_z = 0.1219$, $b_z = 21.526$; $a_\theta = 0.0984$, $b_\theta = 13.02$).

In addition to the tip loss phenomena, a stall delay approach was incorporated to account for the 3D influence of rotational flow. This model delays the onset of flow separation by calibrating the 2D lift and drag coefficients, improving the accuracy of aerodynamic performance predictions, particularly under high wind conditions where stall effects are predominant. While the turbines analyzed in the main study do not operate in fully stalled conditions, the stall delay model was incorporated as part of the validation process, as detailed in (Amoura et al., 2025). This validation was conducted on the well-documented NREL Phase VI wind turbine, leveraging its extensive experimental dataset across attached, separated, and stalled flow regimes at wind speeds of 7 m/s, 9 m/s, and 15 m/s, and was compared to the work of Tadamasa & Zangeneh (2011), using the resulting sound pressure level spectrum as the primary comparison parameter to ensure the robustness of the methodology. Among several correction approaches presented in the literature, the correction methodology adopted by Hamlaoui et al. (2021a; 2024a) has been chosen in this study due to its effectiveness on the aerodynamic performance predictions and flow field reproduction around HAWT rotor compared to existing models.

$$C_l = (1 + f_s)C_{l,2D} \tag{7}$$

$$C_d = (1 + f_d)C_{d,2D} (8)$$

where f_s and f_d are specific functions representing the changes in the lift and drag coefficients. $C_{l,2D}$ and $C_{d,2D}$ represent the two-dimensional lift and drag coefficients. The correction approach for these aerodynamic coefficients, introduced by Hamlaoui et al. (2021a) has been expressed as follows:

$$f_s = a \left(1 - \left(\frac{r}{R} \right)^2 \right) exp \left(- \left(\frac{AoA - \alpha_s}{d} \right)^2 \right) \tag{9}$$

$$f_d = a_h \left(\frac{c}{r}\right)^h \cos^n(\beta) \tag{10}$$

where a, α_s and d are constants equal respectively to 1.8, 25 and 9.5, representing the amplitude, the 3D delayed stall AoA and the controlling peak width. Additionally, the proposed constants a_h , h and n have been set to the values of 1.2, 1 and 4 respectively.

Finally, the closure of the algebraic system is accomplished using the two-equation k- ε turbulence model, represented by the following expressions:

$$\frac{\partial (\rho k)}{\partial t} + \frac{\partial (\rho k u_i)}{\partial x_i} = \frac{\partial}{\partial x_j} \left[\left(\mu + \frac{\mu_t}{\sigma_k} \right) \frac{\partial k}{\partial x_j} \right] + P_k + P_b + \rho \varepsilon \tag{11}$$

$$\frac{\partial(\rho\varepsilon)}{\partial t} + \frac{\partial(\rho\varepsilon u_i)}{\partial x_i} = \frac{\partial}{\partial x_i} \left[\left(\mu + \frac{\mu_t}{\sigma_{\varepsilon}} \right) \frac{\partial \varepsilon}{\partial x_i} \right] + C_1 \frac{\varepsilon}{k} (P_k + C_3 P_b) - C_2 \rho \frac{\varepsilon^2}{k}$$
 (12)

where P_k and P_b are respectively, the turbulent kinetic energy production rate due to the mean velocity shear and the buoyancy. ε represents the turbulent kinetic energy dissipation rate, $\mu_t = \rho \ C_\mu \frac{k^2}{\varepsilon}$ is the eddy viscosity as mentioned earlier, and C_1 , C_2 and C_3 are model coefficients whose values are provided in Table1. This turbulence model is widely recognized for its efficiency in capturing key turbulent flow characteristics in regions

such as the turbine wake. Considering the aeroacoustics methodology applied, it provides sufficient details without overwhelming computational resources, making it suitable for large-scale simulations involving multiple wind turbines.

Table 1 k-E turbulence model closure coefficients

Model	σ_k	σ_{ε}	C_1	C_2	C_3
Launder & Sharma (1974)	1.0	1.3	1.44	1.92	0.09

2.2 Aeroacoustics Considerations

This section focuses on the formulation of the aeroacoustics model used to analyze wind turbine noise generation and its propagation. To achieve this, a hybrid aeroacoustics approach is adopted, combining the FW-H acoustic analogy to model the acoustic pressure fluctuations induced by the actuator disk and the unsteady flow interactions. These are then used as source terms in the Linearized Euler Equations (LEE), which simulate farfield sound propagation in a non-uniform atmospheric medium, including reflection, refraction, and diffraction effects, particularly important in complex terrain or varying atmospheric conditions. This hybrid methodology ensures that both near-field and far-field acoustic phenomena are accurately represented, offering a comprehensive framework for assessing wind turbine noise under different operating scenarios and spatial configurations.

2.2.1 Ffowcs Williams-Hawkings acoustic analogy

Acoustic analogies are used to describe the relationship between fluid flow and the acoustic field. The FW-H acoustic analogy, part of the density-based category, is a widely used method for predicting noise generated by turbulent flows, particularly in aerodynamics. The FW-H acoustic analogy extends Lighthill's theory by incorporating the influence of moving surfaces on sound generation. This analogy involves reformulating the continuity and momentum equations by identifying pressure or density fluctuations as the primary acoustic variables, yielding an inhomogeneous wave equation whose source terms encapsulate the physical origins of the sound generation.

$$\begin{split} &\frac{1}{c_0^2}\frac{\partial^2 p'}{\partial^2 t} - \overline{V}\overline{p'} = \frac{\partial}{\partial t}\{[\rho_0 v_n + \rho(u_n - v_n)]\delta(f)\} - \frac{\partial}{\partial x_i}\{[P_{ij}n_i + \rho u_i(u_n - v_n)]\delta(f)\} + \frac{\overline{\partial^2}}{\partial x_i \partial x_j}\{T_{ij}H(f)\} \end{split} \tag{13}$$

where p' represents the sound pressure; ρ the static fluid density, and ρ_0 the initial fluid density in the quiescent medium. The implicit function f(x,t)=0 describes the boundary integral surface, satisfying $\nabla f(x,t)=\hat{n}$ in which \hat{n} denotes the unite normal vector points towards the outside of the integral surface. The fluid velocity in the direction normal to the control surface f=0 is denoted by u_n , while v_n denotes the control surface velocity in the direction normal to the surface. The speed of sound in the undisturbed medium is indicated by c_0 . The Heaviside and the Dirac delta function represented by H(f) and $\delta(f)$, respectively. $T_{ij}=\rho u_i u_j - \sigma_{ij} + (p'-c^2 \rho') \delta_{ij}$ is the

Lighthill's stress tensor, while the compressible stress tensor P_{ij} is represented by $p'\delta_{ij}$.

The right-hand member of the FW-H equation can be interpreted as the addition of three distinct acoustic sources. The first term is a monopole source occurring on the moving surface, often referred to as thickness noise because it is associated with air displacement by the blade's thickness, resulting in changes in pressure distribution along the blade surface, which leads to fluctuations in the boundary layer. The second term related to an acoustic dipole source generated by fluctuating forces acting on the blade surface, it is produced by the interaction between the blades and the surrounding airflow, particularly during changes in angle of attack and blade rotation. The final FW-H term can be interpreted as a quadrupole generated by fluctuating Reynolds stresses within a volume around the body. This last term is often neglected because its magnitude is generally negligible compared to the contributions from other sources.

In this study, it is important to note that the control surface $f(\vec{x},t)=0$ is defined as fictitious permeable spherical surface that encloses the entire wind turbine along with all associated acoustic sources, capturing the required flow field information as proposed by Ffowcs Williams to account for the nonlinearities in the vicinity of a moving surface, eliminating the need for volume integration of quadrupoles beyond the data surface. The resulting acoustic pressure from the permeable FW-H formulation (Eq.11) is derived using the Green's function for the wave equation in an unbounded three-dimensional domain.

$$G(x,t;y,\tau) = \begin{cases} 0 & if \ \tau > t \\ \frac{\delta(\tau - t + r/c)}{4\pi r} & if \ \tau \le t \end{cases}$$
 (14)

where: $g = \tau - t + r/c$, and $r = |\vec{x} - \vec{y}|$ is the distance between the noise source and the receiver. Here (x, t) and (y, τ) are the receiver and the source space-time variables, respectively. Resulting in integral formulation of Farassat 1A.

$$\begin{split} &4\pi p'(x,t) = \int_{f=0} \left[\frac{\rho_0(\dot{U}_n + U_n)}{r(1 - M_x)^2}\right]_{ret} dS + \\ &\int_{f=0} \left[\frac{\rho_0 U_n \left(r \, \dot{M}_r + c(M_r - M^2)\right)}{r^2(1 - M_x)^3}\right]_{ret} dS + \frac{1}{c} \int_{f=0} \left[\frac{\dot{L}_r}{r(a - M_r)^2}\right]_{ret} dS + \\ &\int_{f=0} \left[\frac{L_r - L_M}{r^2(1 - M_r)^2}\right]_{ret} dS + \frac{1}{c} \int_{f=0} \left[\frac{L_r \left(r \dot{M}_r + c(M_r - M^2)\right)}{r^2(1 - M_r)^3}\right]_{ret} dS \end{split} \tag{15}$$

where: $U_i = \left(1 - \frac{\rho}{\rho_0}\right) v_i + \frac{\rho u_i}{\rho_0}$; $L_i = P_{ij} n_j + \rho u_i (U_n - v_n)$ and $L_M = L_i M_i$. The dot notation over a variable implies its time derivative with respect to the source time, which is expressed in term of the retarded time. Subscripts "r" or "n" denote the dot product of the vector with either the unit vector in the radiation direction or the unit vector in the surface normal direction, respectively (Lin & PortéAgel, 2022; Brentner & Farassat, 1998). $M_r = M_j \widehat{r}_j$ represent the components of the source's Mach number vector in the direction of the observer, where $M_j = \frac{v_j}{c}$.

In this study, the control surface is stationary within the fluid domain, leading to $v_i = 0$; $v_n = 0$ and $M_r = 0$, which simplifies the integral formulation.

2.2.2 Linearized Euler Equations

The propagation of wind turbine noise was assessed through a hybrid acoustic methodology, integrating the FW-H acoustic analogy with the LEE for enhanced farfield prediction. This approach enables a clear distinction between sound generation and propagation phases, where the acoustic pressure estimated through FW-H analogy is introduced as a source term within the LEE framework, rather than the general source term \vec{S} represented in Eq. 14. Such formulation transcends the assumption of a homogeneous medium by incorporating all linear interactions between the aerodynamic flow and the acoustic field, effectively accounting for refraction effects and reflections at solid boundaries, which are critical for understanding noise behavior under varying atmospheric conditions. Moreover, by considering the perturbation flow variables to be significantly smaller than the mean flow components, the nonlinear terms in the Euler equations can be omitted, resulting in a simplified yet robust formulation, that can be written as:

$$\frac{\partial \vec{u}}{\partial t} + \vec{V} \cdot \underline{\underline{F}}(\vec{u}) = \vec{S}(\vec{u}) \tag{16}$$

where: $\vec{u} = [p' u_x' u_y' u_z']^t$

$$\underline{F} = \begin{bmatrix} (c_0^2 \rho_0 u_x' + \bar{u}_x p') & (c_0^2 \rho_0 u_y' + \bar{u}_y p') & (c_0^2 \rho_0 u_z' + \bar{u}_z p') \\ u_x' \bar{u}_x + \frac{p'}{\rho_0} & u_x' \bar{u}_y & u_x' \bar{u}_z \\ u_y' \bar{u}_x & u_y' \bar{u}_y + \frac{p'}{\rho_0} & u_y' \bar{u}_z \\ u_x' \bar{u}_z & u_z' \bar{u}_y & u_z' \bar{u}_z + \frac{p'}{\rho_0} \end{bmatrix}$$

$$\vec{S} = \begin{bmatrix} u_x' \left(\frac{\partial \overline{u}_x}{\partial x} + \frac{\partial \overline{u}_y}{\partial y} + \frac{\partial \overline{u}_z}{\partial z} \right) - u_x' \frac{\partial \overline{u}_x}{\partial x} - u_y' \frac{\partial \overline{u}_x}{\partial y} - u_z' \frac{\partial \overline{u}_x}{\partial z} + \frac{p'}{c_0^2 \rho_0^2} \frac{\partial p_0}{\partial x} \\ u_y' \left(\frac{\partial \overline{u}_x}{\partial x} + \frac{\partial \overline{u}_y}{\partial y} + \frac{\partial \overline{u}_z}{\partial z} \right) - u_y' \frac{\partial \overline{u}_y}{\partial x} - u_y' \frac{\partial \overline{u}_y}{\partial y} - u_z' \frac{\partial \overline{u}_y}{\partial z} - u_z' \frac{\partial p_0}{\partial z} \frac{\partial p_0}{\partial y} \\ u_z' \left(\frac{\partial \overline{u}_x}{\partial x} + \frac{\partial \overline{u}_y}{\partial y} + \frac{\partial \overline{u}_z}{\partial z} \right) - u_z' \frac{\partial \overline{u}_z}{\partial x} - u_y' \frac{\partial \overline{u}_z}{\partial y} - u_z' \frac{\partial \overline{u}_z}{\partial z} + \frac{p'}{c_0^2 \rho_0^2} \frac{\partial p_0}{\partial z} \end{bmatrix}$$

The vector \vec{u} denotes the set of unknowns field variables, specifically the acoustic pressure (p') and the velocity perturbation components (u'_x, u'_y, u'_z) , while physical flux $\underline{F}(\vec{u})$ discribe the coupling of these variables, and the source term $\vec{S}(\vec{u})$ has been adjusted here to incorporate the acoustic pressure determined by the FW-H analogy.

3 NUMERICAL MODEL

In the study of noise generation and radiation from wind turbines, a significant challenge arises due to the substantial disparity in length scales between the unsteady aerodynamic flow field and the unsteady radiation acoustic field. This challenge is addressed using the methodology presented earlier in Sec. 2 and Sec. 3. This study examines three main scenarios defined as follows:

• Isolated HAWT: serving as baseline model for the mesh sensitivity analysis in both CFD and CAA, as well as for the noise source parametrization.

- Two co-axially aligned HAWTs: Employed to identify the optimal spacing between the first and the second HAWT arrays, aiming to maximize power output while minimizing noise emissions.
- Three co-axially aligned HAWTs: Applied to establish the optimal distance between the second and third HAWT arrays, with the objective of generalizing spacing results and assessing the feasibility of using noise data from an isolated rotor for aeroacoustics studies across an entire wind farm.

It should be noted that all simulations were performed under identical conditions to ensure comparability across cases.

3.1 Aerodynamic Computations

The proposed methodology consists on ADM simulations performed by solving the URANS equations, coupled with the $k - \varepsilon$ turbulence model. It consists of an in-house subroutine, designated "AD-LGMD", developed by Hamlaoui et al., (2021a & 2022), in OpenFOAM computational framework as a user-defined shared object library. It is based on Finite Volume (FV) discretization of 3D/axisymmetric Navier-Stokes equations in cylindrical coordinates. The AD-LGMD subroutine has been thoroughly validated in previous studies (Hamlaoui, et al., 2021a; 2021b; 2022; 2024a; Amoura, et al., 2025), demonstrating its robustness and accuracy in reproducing the primary aerodynamic characteristics of rotor flows, thereby confirming its suitability for wind turbine performance prediction. The numerical simulations have been conducted on the New Mexico three-bladed 4.5 m diameter HAWT. The rotor blade is constituted of three distinct airfoil profiles mounted along the blade span as follows: The DU91-W2-250 airfoil is applied from 20% to 46% of the blade span, the RISØ-A1-21 airfoil is used from 54% to 66% where the NACA 64-418 airfoil is applied from 74% to 100% of the rotor blade span (Schepers et al., 2012).

The computational domain, as depicted in Fig. 1, used for the aerodynamic simulations is a wedge with radius of 10R, ensuring a low rotor blockage ratio. The inlet is positioned at a distance of 9R upstream from the rotor center where the outlet is located at a distance of 11R in the downstream direction. Whereas, the addition of multiple HAWT rotors consist on maintaining the same

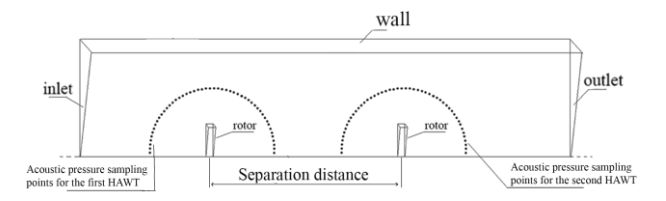


Fig. 2 Aerodynamic computational domain, boundary conditions, and acoustic pressure data acquisition location

inlet and outlet distances from the first and the last rotors and varying the separation distances between them according to the simulation case. Moreover, it should be noticed that the nacelle, with its real geometry, as specified in Table 1 has been taken into consideration during the ADM calculations. The computational domain has been discretized using O-type mesh structure composed of hexahedral cells over the entire domain and prismatic elements concentrated near the rotational axis. In order to ensure accurate predictions in areas with significant flow gradient variations (in the vicinity of the rotor), refined mesh regions of 2R, in both the axial and radial directions, has been defined (see Fig. 2).

Although the Mach number for most HAWT blades remains well below the compressibility threshold, the rhoPimpleFoam solver for compressible flows was employed to address the URANS equations in order to derive the fluctuating parameters required for modeling the FH-W term sources. The mesh sensitivity study, as detailed in Appendix.1, revealed that an actuator elements of 215 point along the rotor blade span, combined with a D/64 resolution in both upstream and downstream regions from the rotor, achieves an optimal balance between accuracy and computational efficiency, delivering accurate torque and velocity distribution while keeping mesh requirements to a minimum (see Fig. 2).

3.2 Aeroacoustics Computations

The dynamic library *libAcoustics*, originally developed by Epikhin et al. (2015), has been integrated into the OpenFOAM environment to extract acoustic pressure data at specified observation points using the integral formulation of the FW-H analogy. The library functions in conjunction with the basic solvers allows the estimation of the required flow features utilizing real-time solution data (Epikhin, 2021). In order to capture accurately the directional dependencies of sound radiation

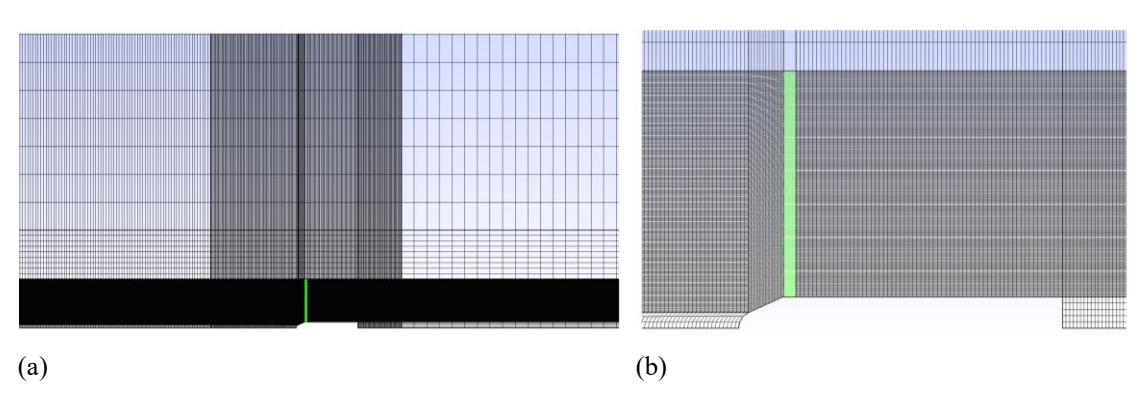


Fig. 1 Mesh Distribution on the Cross-Section of: (a) the Computational Domain Near the HAWT (b) the Wind Turbine

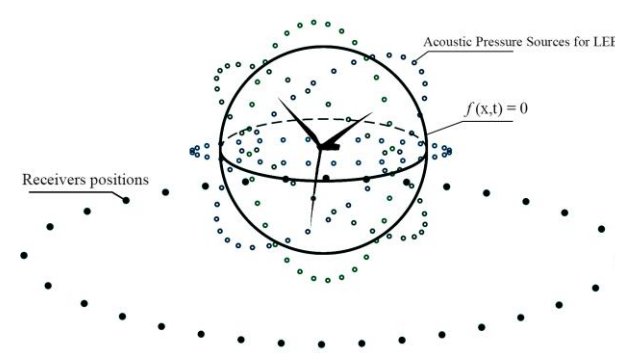


Fig. 3 Acoustic Pressure Sampling Points and Receiver Positions

Table 2 Nacelle and Nose Cone Geometry

Component	Description
Nacelle	Simplified as cylinder, 1/72 geometry Length: 250 cm Radius: 27.5 cm
Nose Cone	Simplified as frustum and half sphere, 1/72 geometry Frustum length: 40 cm Half sphere radius: 15 cm

and maintain the multipolarity nature of noise sources, pressure measurements must be acquired at various locations surrounding the wind turbine, as shown in Fig. 3, which illustrates the placement of pressure sampling points and receivers. These data points are treated as discrete point sources serving as inputs to solve the LEE for far field predictions.

The LEE are subsequently solved using the Discontinuous Galerkin Finite Element Method, as implemented in the high-order CAA solver developed by Khelladi (2024), which supports advanced spatial discretization schemes. This solver offers multiple methods for time integration as: the forward Euler method and the fourth-order Runge-Kutta method. It is also built based on two types of boundary conditions: slip boundaries, which prevent acoustic waves from penetrating the wall, and absorbing boundaries which prevent reflection by absorbing incident waves.

Furthermore, the solver efficiently handles multiple acoustic sources simultaneously affecting significantly the computational time. The schematic diagram illustrating the computational methodology adopted for both aerodynamic and aeroacoustics study is summarized in Fig. 4.

It should be noted that in order to conduct accurate aeroacoustics analyses, particular attention must be provided the aerodynamic noise sources modeling, encompassing both tonal and broadband components. generally, The Nyquist sampling theorem requires that the sampling frequency must be at least twice the highest frequency of interest to prevent aliasing effects and ensure proper resolution. To this end, a sampling frequency of 4 kHz was chosen, which is sufficient to capture the most significant noise components, as these typically occur below this threshold. The blade passing frequency and its harmonics, which dominate tonal noise, generally fall within the range of 1-100 Hz. Additionally, broadband noise, primarily generated by turbulence and flow interactions around the rotor blades, spans a wider frequency range but is most significant in the low to midfrequency range.

The CAA simulations have been carried out across multiple scenarios. For the isolated HAWT case, the computational domain has been modeled as a disk concentric with the acoustic sources, while in other cases, the noise sources have been adjusted to reflect specific separation distances. The CAA mesh sensitivity study has been conducted in a 2D free-field environment. The computational domain has been divided into two regions: the acoustic domain, representing the air surrounding the HAWT where sound propagation occurs, and a buffer zone designed to damp sound waves propagation out of the physical domain. Surrounding the buffer zone, non-reflecting boundary conditions were applied to allow the transmission of outgoing waves without reflection.

A comprehensive mesh sensitivity analysis of the aeroacoustics simulations was provided in details in the second part of the Appendix.1 where the temporal term was computed using the fourth-order Runge-Kutta method for high fidelity time integration. The findings demonstrate that an element size of 1 meter achieves a satisfactory level of accuracy while maintaining computational efficiency,

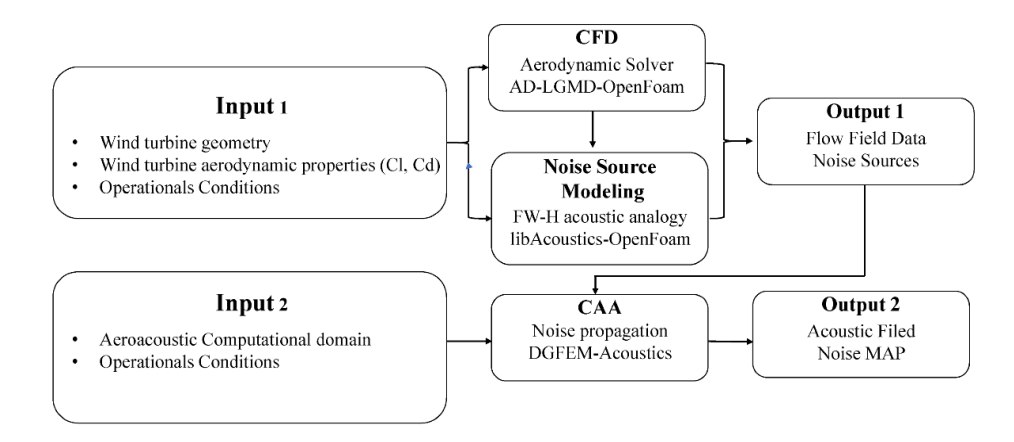


Fig. 4 Proposed scheme of the Aeroacoustics Prediction Methodology

where the overall sound pressure level values exhibit minimal variation among element sizes of 1.5, 1, and 0.5 meters, suggesting that additional refinement would not produce substantial improvements.

4 RESULTS AND DISCUSSION

This research examines the impact of spacing between co-axially aligned New-MEXICO HAWT, subjected to uniform flow conditions, on their aerodynamic performances, noise generation and propagation, aiming to optimize the trade-off between maximizing energy production and reducing noise emissions. Simulations have been carried out under identical operating conditions with an incoming wind speed of $U_0 = U_{Design} = 15 \, m/s$, corresponding to the MEXICO HAWT's optimal operating condition. For this purpose, the research is structured as follows:

- Firstly, various TLCF have been analyzed to identify the most appropriate model allowing better reproduction of the blade loads as well as the flow field around HAWT rotor. The aerodynamic results were validated using extensive datasets from experimental measurements reported in well documented studies (Boorsma & Schepers, 2014; 2016). Additionally, noise source parametrization has been performed to determine the optimal noise sources number required for accurate reproduction of the HAWT noise. Then, validation of the aeroacoustics methodology adopted has been thoroughly conducted on the NREL Phase VI within prior studies, as detailed in prior research (Amoura et al., 2025) for further reference.
- Secondly, aeroacoustics analysis of two co-axially positioned HAWTs has been conducted to determine the optimum spacing of the second HAWT array.
- A third rotor has been introduced to establish the optimal spacing between the second and third HAWT arrays, with the objective of generalizing spacing recommendations.
- Finally, the study assessed whether noise data from an isolated rotor could be effectively applied to aeroacoustics modeling of an entire wind farm.

4.1 Isolated HAWT Case

To identify the appropriate tip loss correction factor for accurately capturing the aerodynamic performance of a HAWT, several simulations have been conducted on a single HAWT using three distinct correction factors namely: Glauert (1963), Shen et al (2005), and Wimshurst and Willden (2017). TLCFs are crucial because they address specific aerodynamic phenomena that occur at the blade tips, such as the formation of tip vortices and the resulting spanwise flow, which can alter the local pressure distribution. Without these corrections, the predicted forces (torque and thrust) may deviate significantly from experimental measurements, especially at high tip speeds.

To test the performance of each TLCF, simulations have been conducted across three different incident wind speeds, of 10m/s, 15m/s and 24m/s corresponding to tip

speed ratios(λ) of 10, 6.67, and 4.17, respectively. The results, presented in Table 3, reveal distinct variations in predicted torque and thrust values, which were compared with experimental data to assess accuracy.

For the lowest wind speed $(U_0 = 10 \text{ m/s})$, Shen's correction factor significantly over-predicted torque by 57%, while Glauert's factor also produced a notable overestimation (55%). In contrast, Wimshurst and Willden's correction factor demonstrated much closer alignment with the experimental data, showing only a 36% shift. Regarding thrust, all three factors produced relatively small deviations, with Wimshurst and Willden's factor presenting almost no shift (0.2%), while Shen's and Glauert's factors showed small but more pronounced differences (1.0% and 12.3%, respectively). At $U_0 =$ 15m/s, the performance of Shen's and Glauert's factors remained similar, with Shen's factor overestimating torque by approximately 13% and Glauert's by 15%. However, Wimshurst and Willden's factor was nearly in perfect agreement with the experimental results, yielding a torque shift of only 1.4%. The thrust values showed even smaller discrepancies across all correction factors, confirming the robustness of the thrust predictions in this case. For the highest wind speed $(U_0 = 24m/s)$, the results diverged further, with Shen's factor overestimating torque by 11%, while Glauert's prediction was within 2% of the experimental value. Wimshurst and Willden's factor once again yielded the most accurate results, with only a 1.6% shift from the experimental torque value. However, the thrust was overestimated by all correction factors, with the largest shift observed for Shen's factor (15.5%).

The analysis of both axial and tangential forces per unit span distribution along the blade, depicted in Fig. 5, further validates these findings. Wimshurst and Willden's factor consistently demonstrated superior accuracy across various wind speeds, which can be attributed to its enhanced recalibration of Shen's tip loss correction model. This approach allows for separate corrections of tangential and axial forces, thereby improving the accuracy of both torque and thrust predictions.

For the acoustic analysis, a comparative study has been conducted to evaluate the convergence of the proposed method and identify the optimal number of sampling points required for accurately representing wind turbine noise generation. This analysis examined the sensitivity of the noise amplitude to the number of sources, gathering fluctuating acoustic pressure data around the wind turbine for five different configurations using the Frassate 1A formulation. Aerodynamic simulations have been performed with sets of 4, 8, 16, 48, and 80 sampling points around an isolated New-MEXICO HAWT subjected to a wind speed of 15 m/s. These points were treated as discrete acoustic sources for resolving the LEE as discussed in section 2.

Given the axisymmetric nature of the ADM, twodimensional acoustic simulations were conducted by duplicating the number of extracted punctual sources, such that each opposing source pair with respect to the axis of rotation yields equivalent acoustic pressure responses. Consequently, acoustic simulations have been carried out

	U=10 m/	's; λ=10	U=15 m/s	s; λ=6.675	U=24 m/s; λ =4.17				
	Q[Nm]	T[N]	Q[Nm]	T[N]	Q[Nm]	T[N]			
EXP	68	974	316	1663	715	2172			
Shen	106.746	983.75	356.775	1659.413	793.264	2508.235			
Glauert	105.378	1094.112	363.021	1680.847	730.152	2269.087			
Wimshust	92.768	972.072	311.634	1661.652	703.362	2518.373			
Shift (%) Shen	56.979	1.001	12.904	0.216	10.983	15.48			
Shift (%) Glauert	54.967	12.332	14.8801	1.073	2.119	4.469			
Shift (%) Wimshust	36.424	0.1979	1.381646	0.081	1.628	15.947			
for various sets of point sources, including 8, 16, 32, 96, and 160 distinct sources.									

Table 3 Torque and thrust values: comparison of different tip loos correction factors

First of all, the Overall Sound Pressure Level (OSPL) has been evaluated by integrating the Sound Pressure Level (SPL) over the frequency spectrum measured downstream of the wind turbine at designated receiver locations, as outlined in the IEC 61400-11 (2012) (International standard IEC/TC 88.61400-11 Ed.2, 2012). The reference distance for this measurement is defined as the sum of the turbine's rotor radius and tower height, here estimated as 7.25m. Table 4 presents the OSPL value derived at this reference distance as a function of the number of noise sources. Additionally, it includes the shift value relative to the case whit the highest number of noise sources (Eq. 20). Results indicate that using 32 noise sources provides a balanced trade-off between computational cost and accuracy, with minimal improvements in accuracy observed beyond this number of acoustic sources.

$$f_{shift}(i) = \left| \frac{o_{SPL(i)} - o_{SPL(160)}}{o_{SPL(i)}} \right| * 100$$
 (17)

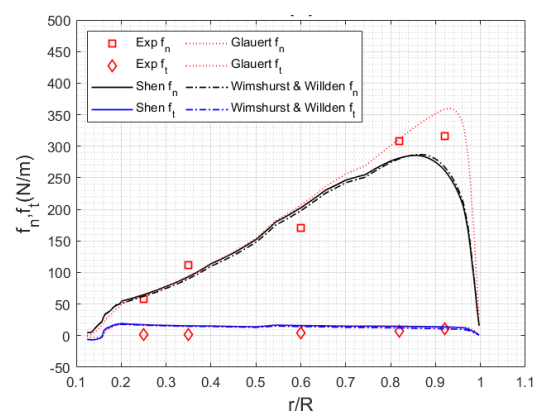
Table 4 Overall sound pressure level value derived downstream a single HAWT at the reference distance

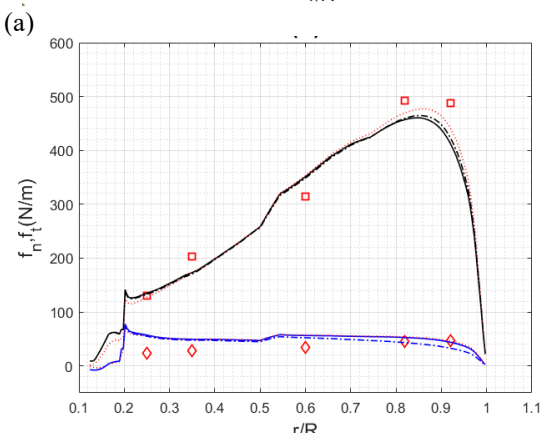
Sources number	8	16	32	96	160
OSPL [dB]	70.74	72.92	78.42	80.03	79.3
f _{shift} (%)	12.1	8.75	1.12	0.91	/

The Sound Power Level (SWL) has been estimated based on OSPL measurements taken from various equidistant positions surrounding the wind turbine, according to the international standard ISO 3744 (International Standard ISO 3744, 2010). These positions were selected sufficient distance from the wind turbine, allowing the propagated wave to behave as a plane wave and enabling the use of the following formulation:

$$SWL = 10 \log \left[\frac{1}{N} \Sigma_{i=1}^{N} \ 10^{0.1 \ OSPL_i} \right] - K_1 - K_2 + 10 \log \left(\frac{s}{s_0} \right) \ \ (18)$$

where: N is the number of receptors, K_1 the background noise correction and K_2 represent the test environment correction, s_0 is a reference area taken as $s_0 = 1 m^2$. In this study, both K_1 and K_2 are set to zero as experimental corrections are not applied in our case.





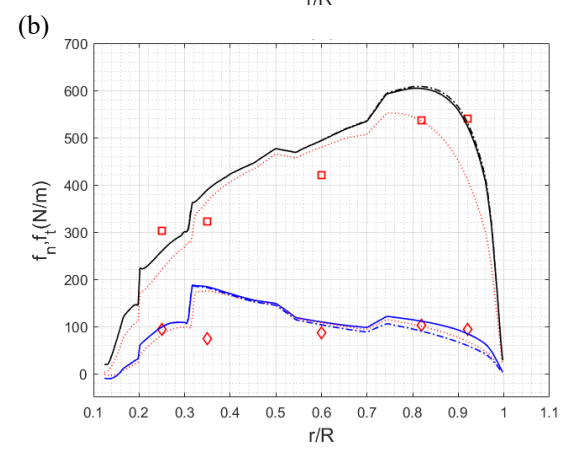


Fig. 5 Axial and tangential forces per unit span distribution for different tip speed ratios (a) $\lambda = 10$, (b) $\lambda = 6.67$, (c) $\lambda = 4.17$

For further accuracy, the OSPL measurement positions were consistently maintained at a distance of 50 meters relative to the domain's geometric center for all

configurations. Moreover, alongside with the Average Sound Pressure Level (ASPL), Table 5 illustrates the SWL estimated from OSPL measurements taken at this distance around the wind turbine. The results revealed minimal discrepancies across different configurations, suggesting that increasing the number of sources had a limited impact on overall noise levels. Therefore, the configuration with 32 sources has been selected as the optimal setup for further simulations.

Table 5 ASPL and SWL of a Single HAWT as a Function of Noise Source Number

Sources number	8	16	32	96	160
ASPL [dB]	70.44	70.11	72.88	74.45	73.94
SWL [dB]	115.41	115.08	117.85	119.42	118.91

In addition to assessing these sound levels, it is critical to evaluate the directional characteristics of the emitted noise. Wind turbine noise is often exhibiting a nonuniform diffusion pattern, strongly influenced by directional proportionality, which impacts noise perception at different positions around the wind turbine. To capture this directional behavior, OSPL measurements were taken at equidistant points surrounding the turbine, at a distance twice the reference distance. This choice was made to mitigate attenuation effects caused by geometric divergence while ensuring sufficient wave propagation for reliable assessment, providing a comprehensive view of noise radiation across different directions. The results, shown in Fig. 6, clearly illustrate the anisotropic distribution of the overall sound pressure levels around the HAWT. The polar plot reveals a distinct dipolar pattern, characterized by two pronounced lobes of elevated noise levels observed primarily in the upwind and downwind directions, coinciding with the turbine's rotational axis. Conversely, significantly lower noise levels are detected in the perpendicular direction, reflecting the inherently directional nature of wind turbine noise emissions. This anisotropic distribution suggests that the noise intensity is not only a function of the turbine's operational parameters, such as rotational speed and blade design, but also heavily dependent on the receiver's relative position with respect to the turbine, revealing the importance of the directional analysis for understanding the environmental impact of wind turbine noise.

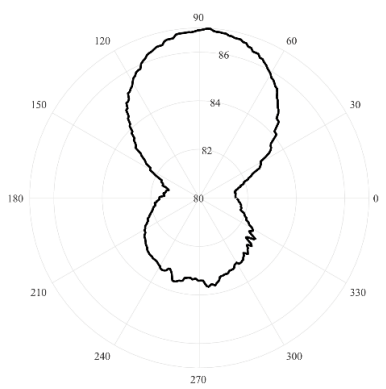


Fig. 6 OSPL Directivity recorded at a spacing of twice the reference distance from the wind turbine

4.2 Tow Co-axially Positioned HAWT Case

In order to investigate the effects of separation distance on noise generation between two aligned HAWT, a series of simulations have been conducted. These simulations explored various turbine configurations, focusing on how spacing influences aerodynamic performances and noise generation. Noise sources were modulated and analyzed around each turbine to evaluate the specific contribution to the total noise emitted. Three separate acoustic simulations were conducted for each configuration, focusing on the propagation of wind turbine noise. The first two scenarios simulate the noise generated by the first and second HAWTs individually, while the third scenario models the case where both turbines operate simultaneously. To ensure consistency, the receiver positions were kept the same across all scenarios, as described in Section 4.1. Sound pressure levels were measured at a distance of 50 meters from the origin of the domain (Fig. 7), providing a standardized baseline for comparison.

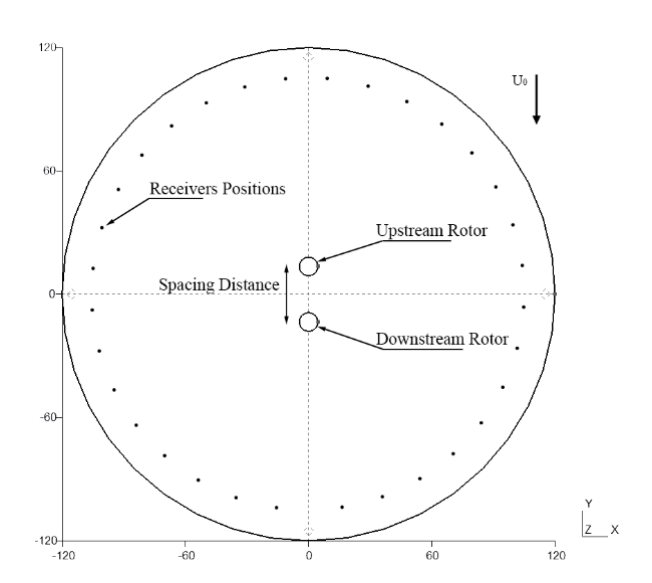


Fig. 7 Acoustics's Computational Domain

Wind turbines naturally create wake regions of turbulent airflow downstream of the rotor blades, which contain vortices and turbulence that significantly impact both the aerodynamic and acoustic performance of nearby turbines. For aligned turbines, the wake from an upstream turbine disrupts the airflow around the downstream turbine, reducing its aerodynamic power generation while also altering its acoustic signature and impacting noise emitted. Additionally, sound waves from multiple turbines can overlap, resulting in either constructive or destructive interference depending on their relative phases, which is strongly influenced by the separation distance. When turbines are closely spaced, their acoustic fields can either reinforce or cancel each other, leading to variations in noise levels. If the separation distance varies along a straight line, the interference pattern often exhibits periodicity. This periodic behavior means that certain distances lead to amplified noise levels due to constructive interference, while others result in reduced noise due to destructive interference.

In the present study, the aerodynamic and aeroacoustics performances of both wind turbine rotors, were assessed through the power output and the corresponding SWL, which were analyzed across varying separation distances. The results demonstrate a clear correlation between spacing distance and both aerodynamic efficiency and noise generation, particularly for the downstream turbine.

The power loss, as defined in Eq. 22, decreased from 0.687 at a separation distance of 3D to 0.446 at 8D, reflecting a considerable gain in energy captured by the downstream rotor. Unfortunately, this improvement in power output is accompanied by a notable increase in noise generated by the downstream turbine, as indicated in Table 6, where the SWL rose from 111.47 dB at 3D to 117.48 dB at 8D. This rise can be attributed to the enhanced flow-rotor interaction in the wake recovery zone, which amplifies noise levels as the flow velocity increased, underscoring the direct relationship between wake recovery and noise emission.

$$C_{p \ loss} = \frac{c_{p \ upstreamRotor} - c_{p \ downstreamRotor}}{c_{p \ upstreamRotor}}$$
(19)

Table 6 Power delivered and SWL for each HAWT as a function of spacing distance

	Upstream Rotor		Downstrea		
Spacing Distance	Power [W]	SWL [dB]	Power [W]	SWL [dB]	Power Loss rate
3D	13306.6	124.03	4164.39	111.47	0.687
4D	13389.48	121.37	4989.22	109.43	0.627
5D	13746.74	122.71	5948.76	112.81	0.567
6D	13742.21	123.34	6537.65	115.78	0.524
7D	13737.17	121.84	6993.32	110.85	0.491
8D	13737.6	121.6	7610.4	117.48	0.446

The axial velocity distribution illustrated in Fig. 8, further highlights the impact of wake recovery on downstream performance. At shorter distances, such as 3D and 4D, the downstream turbine operates in a highly disrupted flow region, characterized by significant velocity deficits that limit aerodynamic interactions, reducing both power output and noise generation. As the spacing increases to 6D or 7D, the wake recovery is more complete, resulting in a smoother and higher incoming flow velocity to the downstream turbine. This enhanced inflow improves aerodynamic efficiency but also rotor-structure amplifies noise due to stronger interactions. This finding highlights the trade-off between energy efficiency and noise emission, which is particularly critical for wind farm design, where both performance and environmental impact must be balanced. Theoretically, achieving full recovery of the downstream turbine's power output would require an infinite separation distance (Choi, 2013). However, in practical terms, industry standards recommend a separation distance of approximately five times the rotor diameter (5D), as it represents a point where the wake's strong influence is largely diminished. This standard is also influenced by the increased costs associated with energy transition and the need to optimize

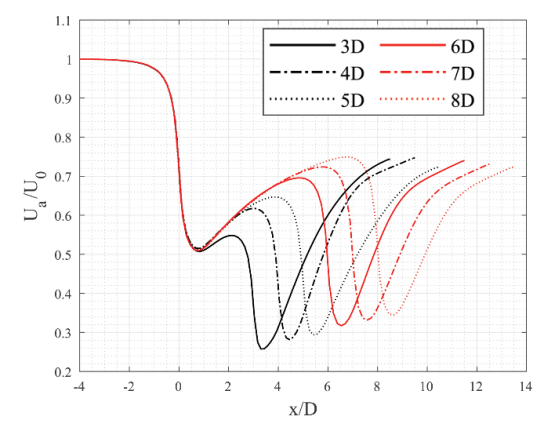


Fig. 8 Axial velocity distribution as a function of spacing distance obtained at a radial station of r=1.5m

land use in wind farm layouts.

The noise generation of a downstream wind turbine in an aligned configuration is also shaped by the turbulent kinetic energy (TKE) retained in the upstream wake. As the wake evolves, turbulent structures formed by tip vortices and shear layers produce fluctuating aerodynamic forces on the blades, leading to broadband noise through rapid pressure variations. With increased spacing, this turbulence progressively decays and becomes more diffused (see Fig. 9), which can reduce the contribution of turbulence-induced broadband noise. However, the concurrent rise in mean inflow velocity continues to intensify the aerodynamic loading and unsteady rotorflow interactions responsible for higher noise levels. Accordingly, tonal noise components associated with periodic blade-passing frequencies tend to remain relatively unaffected by the decay of turbulence intensity. Therefore, the overall noise at the downstream turbine results from a complex interplay: while decreasing turbulence intensity reduces unsteady loading noise, the enhanced velocity and stronger rotor-flow interaction due to wake recovery increase aerodynamic noise.

The upstream turbine demonstrated relatively stable noise levels (SWL), ranging from 121.37 dB to 124.03 dB, across different spacing distances. This variation suggests minor interference effects, likely influenced by acoustic wave interactions with the downstream turbine. The slight fluctuations in SWL may result from constructive and destructive interference patterns arising from overlapping sound waves, though the upstream turbine's noise levels appear less sensitive to spacing distance compared to the downstream turbine.

By comparing the cumulative noise levels from the first two scenarios and the third one, it is evident that the combined noise levels from both turbines often deviate from the logarithmic sum of the individual noise levels. This discrepancy underscores the significant role of the acoustic interference phenomena in shaping the overall noise distribution during the wave's propagation.

Furthermore, the accumulated SPL spectra for different spacing cases, measured at the same downstream location, exhibit a consistent spectral behavior across all cases.

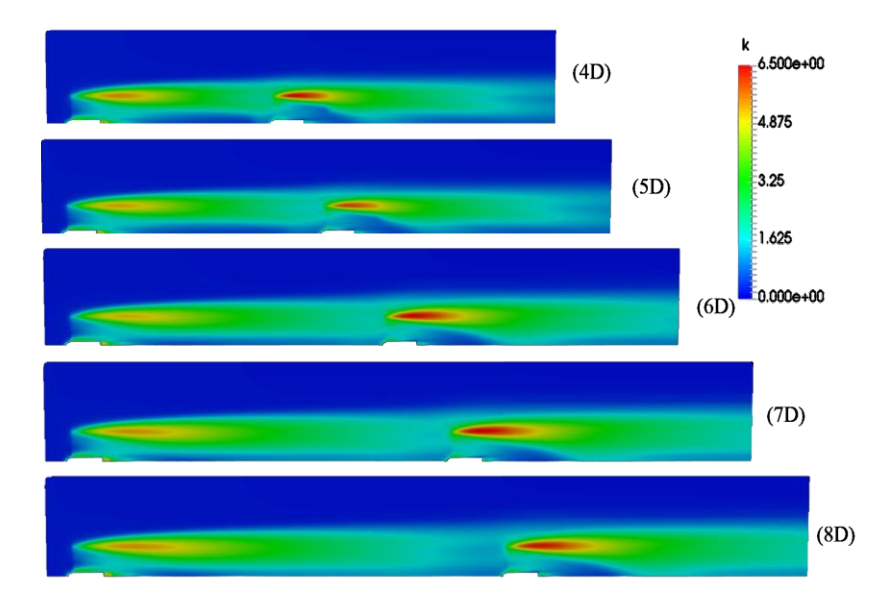


Fig. 9 Turbulent kinetic energy distribution for different turbine spacing distances

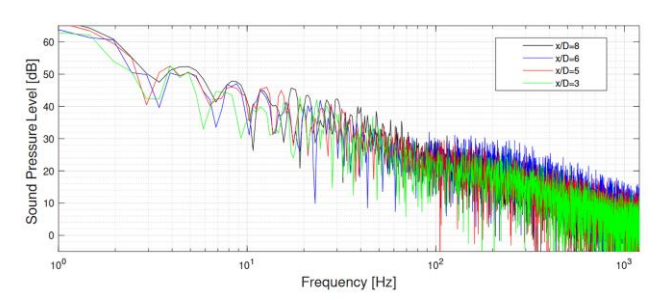


Fig. 10 Comparison on SPL spectra for different spacing cases

As depicted in Fig. 10, the tonal peak positions remain unchanged, indicating that the dominant frequency components of the noise remain unaffected by the spacing distance. However, variations in SPL amplitude are observed, influenced not only by wake recovery but also by interference effects, which introduce a periodic pattern in the overall noise levels. The total Sound Power Level (SWL) values in Table 7 highlight this periodic behavior, where the SPL does not increase monotonically with spacing. For instance, while a larger separation generally enhances wake recovery and increases power output, the 4D spacing case results in a higher SWL than the 5D case, before rising again at 6D and beyond. This suggests that constructive and destructive interference between noise sources plays a crucial role, modulating the overall noise emissions in a non-linear manner. These findings highlight the complexity of noise prediction in multi-turbine configuration, where spacing adjustments may not yield straightforward noise mitigation. The periodic nature of

Table 7 Total power delivered and noise emitted as a function of spacing distance

Spacing Distance	3D	4D	5D	6D	7D	8D
Total SWL	120	123.	123.	122.	123.	124
[dB]	.47	98	72	35	43	.74
Total Power	174	1837	196	2027	2102	213
Output[W]	71	8.69	95.5	9.85	1.88	48

these interference effects suggests that wind farm designers must carefully consider specific spacing distances to effectively manage and control overall noise emissions.

The main objective of this study was to reconcile energy production and noise reduction, by identifying the optimal operational margin for the system. To achieve this, a multi-optimization study has been undertaken using the Particle Swarm Optimization (PSO) algorithm to determine this ideal separation distance. However, since the problem involves two competing objectives (power generation and noise reduction) but only single variable (turbine separation distance), the outcome naturally forms a Pareto front, where no single solution fully satisfies both objectives. In such cases, enhancing one objective typically leads to compromise the other, preventing a unique, optimal solution from being identified. To overcome this challenge, a scalarization approach has been adopted, simplifying the multi-objective problem by converting it into a single function. This was achieved by combining the power coefficient and SWL into a weighted sum, effectively addressing the trade-offs between aerodynamic performance and noise generation. This approach allowed for a more straightforward and practical solution, eliminating the complexity of multi-objective optimization while still providing a balanced outcome between energy production and noise control.

Initially, both parameters were scaled to ensure comparability, utilizing the standardization method expressed as follows:

$$SWL_{scaled} = \frac{SWL_{Origineal} - mean_{SWL}}{Standard\ Derivation_{SWL}}$$
 (20)

$$Power_{scaled} = \frac{{}^{Power_{Original} - mean_{Power}}}{{}^{tandard\ Derivation_{Power}}} \tag{21}$$

Mathematical expressions for the cumulative power output and total sound power level as functions of spacing distance were derived from simulation data using logarithmic and polynomial regressions, respectively:

$$Power_{scaled}\left(\frac{x}{D}\right) = 3.922 \ln\left(\frac{x}{D}\right) - 6.9015 \tag{22}$$

$$SWL_{scaled}\left(\frac{x}{D}\right) = -0.3081 \left(\frac{x}{D}\right)^4 + 7.5359 \left(\frac{x}{D}\right)^3 - 67.208 \left(\frac{x}{D}\right)^2 + 258.54 \left(\frac{x}{D}\right) - 361.811 \quad (23)$$

These equations have been used to construct the final objective function, given by:

$$f_{obj}\left(\frac{x}{D}\right) = \omega * Power_{scaled}\left(\frac{x}{D}\right) - (1 - \omega) * SWL_{scaled}\left(\frac{x}{D}\right)$$
 (24)

where ω is the weighting coefficient that determines the relative significance assigned to aerodynamic performance (power output) and noise generation. The choice of ω directly influences the optimization results, shaping the trade-off between maximizing energy capture and minimizing acoustic emissions. Figure 11 illustrates the variation of the objective function across different turbine spacing distances x/D for different values of ω . The results reveal distinct trends based on the assigned weighting:

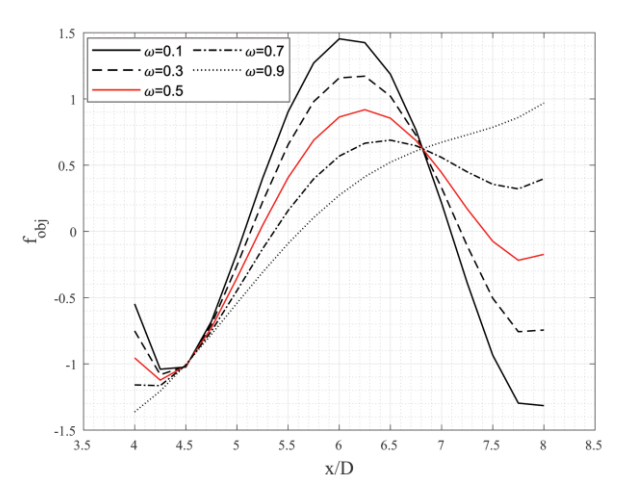


Fig. 11 Objective function variation of two aligned HAWTs versus spacing distance

- For lower values of ω (e.g., $\omega = 0.1$,0.3), where noise reduction is prioritized, the objective function reaches its peak near 6D before declining. This indicates that beyond this spacing, the aerodynamic benefits of wake recovery are outweighed by the increasing noise penalty.
- For moderate values ($\omega = 0.5$), which assign equal importance to power generation and noise mitigation, the objective function attains its maximum at 6.5D. However, the difference between 6D and 6.25D remains minimal, with only a 0.82% drop in power output and an almost negligible 0.02% increase in noise levels. Given these minimal variations, 6D is identified as the most practical choice, ensuring efficient energy capture while maintaining acceptable noise levels.
- For higher values of ω (e.g., $\omega = 0.7, 0.9$), where aerodynamic performance takes precedence, the optimal spacing shifts toward 8D. This reflects the greater importance assigned to power extraction, as wider spacing allows for enhanced wake recovery.

However, this gain comes at the cost of increased noise levels, which are deprioritized in these cases.

The choice of ω significantly influences turbine spacing optimization. While higher values favor aerodynamic performance, pushing the optimal distance to 8D, an equal weighting ($\omega = 0.5$) balances power output and noise constraints, making 6D the optimal compromise. This selection ensures efficient energy production while keeping noise levels within acceptable limits, offering a practical guideline for wind farm design.

4.3 Three Co-axially Positioned HAWT Case

Having established an optimal separation distance of 6D between two co-axially aligned HAWTs that effectively reconciles both aerodynamic performance and noise generation, the next phase involves extending these findings to a more complex and less favorable scenarios. The objective is to identify an ideal separation distance for a wind farm layout that encompasses multiple turbines, focusing on maintaining both efficiency and minimal noise impact. A crucial configuration for investigation is the alignment of three HAWTs, as the additional turbine introduces new interactions, particularly between the second and third rotors. These interactions are likely to influence the overall performance of the wind turbines array. The aim is to assess whether the previously determined 6D spacing between the first and second turbines remains optimal with a third turbine, or if adjustments are needed to maintain the balance between power output and noise generation. To address this, a new study has been conducted in which the 6D separation distance between the first and second turbines was held constant, while the distance between the second and third turbines was varied to assess its impact.

Aerodynamic performance was assessed measuring the total power output from all three turbines, while total noise emissions were quantified using the cumulative SWL. This consistent approach, in line with prior analyses, ensures that contributions to both power and noise from all turbines are comprehensively accounted for. The results indicate that varying the spacing between the second and third turbines significantly impacts the total noise generated, as shown in Table 8. Both the ASPL and SWL values exhibit a proportional relationship with the spacing distance. This finding aligns with the trends seen in the two-turbines configuration. Positioned furthest downstream, the third turbine operates within a flow heavily influenced by the wakes of the upstream turbines, resulting in a minimal contribution to the total noise compared to the

Table 8 Power delivered and Noise Generated from Three Aligned HAWT in function of the spacing distance

Spacing Distance	Power [W]	ASPL [dB]	SWL [dB]
4D	23797.93	65.57	110.54
5D	24054.59	62.9	107.87
6D	25473.11	66.98	111.96
7D	25633.93	70.82	115.79
8D	25643.9	72.98	117.95

first two turbines. Notably, the inclusion of the third turbine led to a significant reduction in total noise generation across all spacing distances. This reduction is attributable to destructive interference phenomenon, which predominantly impacts the noise generated by the first turbine. However, as the spacing distance increases, the influence of destructive interference diminishes. Specifically, the noise level from the upstream turbine, the primary contributor to overall noise, decreased from 117.8 dB in the single-turbine setup to 114 dB in the final three-turbine arrangement. These findings indicate that interference, particularly destructive interference, is the primary factor influencing noise reduction from the first turbine, thereby shaping the overall noise profile.

Figure 12, provides a visual comparison of acoustic wave propagation in a three-turbine configuration under two spacing scenarios. In the 5D spacing scenario, destructive interference has more pronounced effect on noise emission, as evidenced by the diminished amplitude of acoustic waves propagating outward. In contrast, the 6D spacing scenario exhibits less pronounced destructive interference, leading to relatively higher acoustic pressure. In addition, the contours illustrate strong interference patterns that effectively mitigate noise, particularly downstream, where the overlap of sound waves contributes to enhanced noise reduction. It is important to note that the pressure values presented correspond to instantaneous acoustic pressure perturbations relative to the ambient mean pressure; therefore, both positive (compressive) and negative (rarefactive) values naturally occur as part of the oscillatory acoustic field.

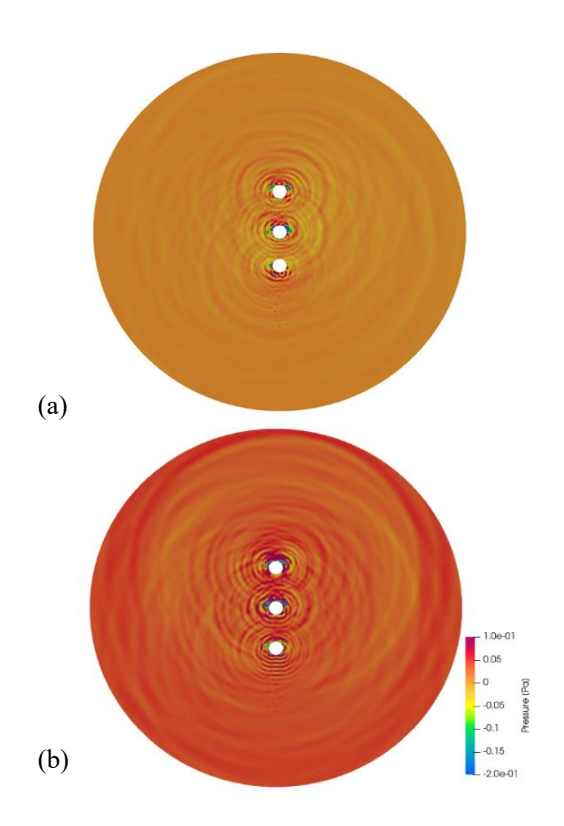


Fig. 12 Instantaneous acoustic pressure propagation [Pa] of the time domain simulation at t=2.5s, corresponding to a spacing distance of:
(a) 5D (b) 6D

Following the same methodology used in previous configurations to determine optimal spacing, mathematical expressions for accumulated aerodynamic power and total noise generation were derived using only polynomial regression. The resulting equations are as follows:

Power_{scaled}
$$\left(\frac{x}{D}\right) = 0.1796 \left(\frac{x}{D}\right)^4 - 4.4434 \left(\frac{x}{D}\right)^3 + 40.246 \left(\frac{x}{D}\right)^2 - 157.11 \left(\frac{x}{D}\right) + 221.55 (25)$$

$$SWL_{scaled}\left(\frac{x}{D}\right) = -0.1941\left(\frac{x}{D}\right)^3 + 3.6795\left(\frac{x}{D}\right)^2 - 21.901\left(\frac{x}{D}\right) + 40.503$$
 (26)

The optimization results for three co-axially aligned turbines confirm previous findings that a spacing distance of 6D remains a robust choice when considering a balanced trade-off between power generation and noise mitigation ($\omega = 0.5$), as shown in Fig. 13. However, when noise reduction is prioritized ($\omega = 0.2$), the optimal spacing shifts to 5D, where the influence of wake interactions helps in dampening acoustic emissions. Conversely, when power output is the dominant factor ($\omega = 0.8$), the optimal spacing increases to 7.5D - 8D, where enhanced wake recovery maximizes energy capture despite higher noise levels. These results indicate that while 6D serves as a practical reference, the optimal spacing distance is sensitive to the weighting of noise versus power efficiency. This refined approach enables more adaptable wind farm layouts tailored to specific environmental and regulatory constraints.

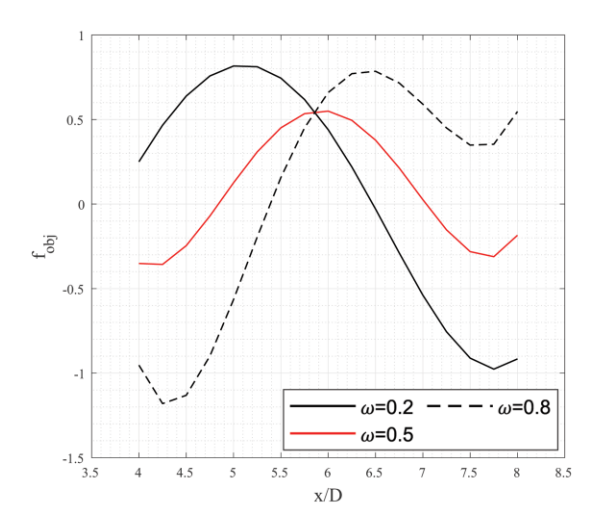


Fig. 13 Objective function of three HAWTs as a function of spacing distance

4.4 Impact of Simplified Noise Modeling on Wind Farm Acoustic Predictions

In multi-objective optimization of wind farm layouts, noise sources are commonly modeled using standardized values provided by the manufacturers, which are based on a wind turbine's predefined operational conditions. These studies frequently rely on the ISO 9613-2 (1996) sound propagation model, an engineering approach for calculating sound attenuation during outdoor propagation to predict environmental noise levels at various distances

from different sources (Kwong et al., 2012 & Nyborg et al., 2023). This section investigates the feasibility of modeling an entire wind farm based on the aeroacoustics analysis of an isolated wind turbine. To explore this, a comparison between two distinct configurations has been performed, employing aeroacoustics simulations of aligned turbines and exploring two approaches of modeling the acoustic sources. In the first configuration, acoustic sources were derived from an aerodynamic simulation of multiple aligned turbines. In the second configuration, acoustic sources were modeled based on an aerodynamic simulation of a single isolated HAWT, applying identical sources across all turbines to streamline the wind farm modeling process while maintaining accuracy. Sound pressure levels were averaged across a set of surrounding sensors to assess the total noise generated by each configuration. The results, presented in Table 9, revealed notable differences in the SWL between these two modeling approaches, especially in threeturbine configuration. For the two-turbine configuration, the SWL discrepancy attend the 2.82 dB, reflecting a moderate yet non negligible difference. This variation indicates the onset of wake effects influencing acoustic behavior, though the simplified single-turbine approach reasonably accurate for less complex configurations. In contrast, when extending the study to a more complex arrangement involving three aligned turbines, a more pronounced difference emerged, reaching 16.11 dB. This substantial discrepancy suggests that the cumulative effect of wake interactions and acoustic wave interference plays a significant role in the noise profile of the wind farm. This pronounced divergence underscores the importance of accurately capturing these effects in multi-turbine configurations, as simplified single-turbine models become less reliable as the number of turbines increases. These findings suggest that detailed simulations accounting for wake interactions and acoustic wave behavior are essential for accurate noise predictions in larger wind farms. Failing to account for these factors may lead to substantial overestimation of noise emissions, with implications for environmental potential impact assessments and compliance with noise regulations.

Table 9 Sound Levels of Multiple Aligned Wind Turbine

	Two Aligne	ed WT	Three Aligned WT		
	Identical Different Sources Sources		Identical Sources	Different Sources	
SWL [dB]	125.17	122.35	128.07	111.96	

Therefore, proposing a new aeroacoustics model capable of precise noise predictions for complex wind farm configurations becomes critical. For future work, we aim to gain a deeper understanding of the various factors influencing noise modeling, with the aim of developing a simplified yet accurate approach. This approach will incorporate correlations for the sound power level predictions as a function of the spacing distance and array size, accounting for wake effects and wave interference. Unlike conventional approach that apply identical noise levels across all turbines, often resulting in substantial

overestimation, this model is commonly used as it represents the worst-case scenario for noise emissions.

5 CONCLUSION

This study provides significant insights into the influence of separation distance between co-axially aligned HAWTs on their aerodynamic performances and noise characteristics under uniform flow conditions, focusing on configurations of two and three turbines, and introducing a hybrid approach for predicting HAWTs noise generation and propagation, based on the Linearized Euler Equations. This approach integrates CFD and CAA through three distinct models. ADM was applied within Reynolds-Averaged Navier-Stokes Unsteady (URANS) framework for capturing the interactions between the rotor and the turbulent flow field. The FW-H analogy further facilitated the coupling of the aerodynamic and aeroacoustics computations, addressing key challenges in noise modeling, by employing the Farassat 1A formulation to estimating the acoustic pressures data, which are processed through the LEE for far-field noise prediction. The validity of this approach was confirmed through comparison with prior research, demonstrating good agreement between the two sets of measurements.

Mesh sensitivity analysis and optimization of acoustic source number required for accurately representing HAWT noise have been performed on an isolated HAWT, reaffirming the dipolar nature of its noise emissions. The study then explored the effect of spacing between two coaxially aligned HAWTs. Results highlighted the substantial impact of wake effects on power output and noise levels for downstream rotor, as well as the occurrence of noise interference between both turbines. A multi-objective optimization study identified a 6D spacing as ideal for balancing energy efficiency and minimizing noise emissions. Expanding the analysis to a three-turbine configuration, while maintaining the optimal 6D spacing between the first two turbines, revealed that varying the distance between the second and third HAWT enhances the destructive interference effect on received noise. These findings further reinforce the designation of 6D as an optimal spacing, as it consistently demonstrates its effectiveness in minimizing noise levels while maximizing aerodynamic performance in multi-turbine arrangements. Finally, this research assessed the feasibility of simplifying wind farm modeling through the application of aeroacoustics analysis based on a single isolated turbine. While this approach provides valuable insights during the early stages of design and analysis, findings highlight the necessity for more detailed simulations in configurations with multiple turbines, where significant wake interactions and acoustic interference phenomenon necessitate a comprehensive aeroacoustics assessment of the entire wind farm array to ensure accurate noise predictions.

Future work will focus on developing a new simplified noise modeling approach that accounts for variations in sound power levels as a function of turbine spacing and array size. This approach aims to enhance both the accuracy and computational efficiency of noise predictions, offering a more comprehensive assessment of wind farm noise impacts. Additionally, while this study focused on a simplified case to establish the proposed methodology, future investigations could incorporate Atmospheric Boundary Layer (ABL) effects to refine wake modeling accuracy. Although the influence of ABL on wake recovery was beyond the scope of this study, its integration into future models will provide a more realistic representation of wind turbine interactions and their acoustic implications.

ACKNOWLEDGEMENTS

The data used have been supplied by the consortium which carried out the EU FP5 project Mexico: 'Model rotor EXperiments In COntrolled conditions.

CONFLICT OF INTEREST

The authors declare no conflict of interest.

AUTHORS CONTRIBUTION

A. Amoura: Writing; A. Smaili: review & editing; S. Khelladi: review & editing; M. N. Hamlaoui: Writing – review & editing; S. Kouidri: review & editing.

REFERENCES

- Amoura, A., Khelladi, S., Smaili, A., & Hamlaoui, M. N. (2022). Toward a Numerical Modeling of Aeroacoustics Noise Induced by Wind Turbine Farm Using Linearized Euler Equations. *International Conference on Advanced Renewable Energy Systems*, (pp. 95–103). https://doi.org/10.1007/978-981-99-2777-7_11
- Amoura, A., Khelladi, S., Smaili, A., & Hamlaoui, M. N. (2025). Validation of a Hybrid Approach for Wind Turbine Noise Prediction Using the Linearized Euler Equations. In *Technological and Innovative Progress in Renewable Energy Systems: Proceedings of the 2024 International Renewable Energy Days (IREN Days' 2024).* (pp. 97–100). Springer. https://doi.org/10.1007/978-3-031-71926-4
- Boorsma, K.; Schepers, J. G. (2014). New MEXICO experiment: Preliminary overview with initial validation. ECN.
- Boorsma, K., & Schepers, J. G. (2016). Rotor experiments in controlled conditions continued: New Mexico. *Journal of Physics: Conference Series*, 753, p. 022004. 753, p. 022004. https://doi.org/10.1088/1742-6596/753/2/022004
- Brentner, K. S., & Farassat, F. (1998). Analytical comparison of the acoustic analogy and Kirchhoff formulation for moving surfaces. *AIAA Journal*, *36*, 1379–1386. https://doi.org/10.2514/2.558.
- Broatch, A., Navarro, R., García-Tíscar, J., & Ramírez, F. N. (2024). Evaluation of different FW-H surfaces and modal decomposition techniques for the acoustic

- analysis of UAV propellers through detached eddy simulations. *Aerospace Science and Technology*, 146, 108956. https://doi.org/10.1016/j.ast.2024.108956
- Cao, J. F., Zhu, W. J., Shen, W. Z., Sørensen, J. N., & Sun, Z. Y. (2020). Optimizing wind energy conversion efficiency with respect to noise: A study on multicriteria wind farm layout design. *Renewable Energy*, 159, 468–485. https://doi.org/10.1016/j.renene.2020.05.084
- Choi, N. J. (2013). Numerical study on the horizontal axis turbines arrangement in a wind farm: Effect of separation distance on the turbine aerodynamic power output. *Journal of Wind Engineering and Industrial Aerodynamics*, 117, 11-17. https://doi.org/10.1016/j.jweia.2013.04.005
- Colas, J., Emmanuelli, A., Dragna, D., Blanc-Benon, P., Cotté, B., & Stevens, R. (2023, June). Exploring the effect of wind farm flow on wind turbine noise propagation through numerical simulations.
- Epikhin, A. (2021). Validation of the developed open source library for far-field noise prediction. Proceedings of the 27th International Congress on Sound and Vibration, Denver, Colorado. https://doi.org/10.5281/zenodo.5906668
- Epikhin, A., Evdokimov, I., Kraposhin, M., Kalugin, M., & Strijhak, S. (2015). Development of a dynamic library for computational aeroacoustics applications using the OpenFOAM open source package. *Procedia Computer Science*, 66, 150–157. https://doi.org/10.1016/j.procs.2015.11.018
- Farassat, F. (2007). Derivation of Formulations 1 and 1A of Farassat. Tech. rep.
- Glauert, H. (1963). Aerodynamic Theory: A General Review of Progress, volume IV, chapter Division L, Airplane Propellers. Aerodynamic Theory: A General Review of Progress, volume IV, chapter Division L, Airplane Propellers. Dover Publications, Inc., New York, NY.
- Global Wind Energy Council. (2024). Global Wind Report 2024. Global Wind Report 2024. https://gwec.net/global-wind-report-2024/
- Grady, S. A., Hussaini, M. Y., & Abdullah, M. M. (2005).

 Placement of wind turbines using genetic algorithms.

 Renewable Energy, 30, 259–270.

 https://doi.org/10.1016/j.renene.2004.05.007
- Hamlaoui, M. N., Bouhelal, A., Smaili, A., & Fellouah, H. (2024a). An Engineering Approach to Improve Performance Predictions for Wind Turbine Applications: Comparison with Full Navier-Stokes Model and Experimental Measurements. *Journal of Applied Fluid Mechanics*, 17, 1379–1397. https://doi.org/10.47176/jafm.17.7.2404
- Hamlaoui, M. N., Bouhelal, A., Smaili, A., Khelladi, S.,
 & Fellouah, H. (2024b). An inverse CFD actuator
 disk method for aerodynamic design and
 performance optimization of Horizontal Axis Wind

- Turbine blades. *Energy Conversion and Management*, 316, 118818. https://doi.org/https://doi.org/10.1016/j.enconman.2 024.118818
- Hamlaoui, M. N., Smaili, A., & Fellouah, H. (2021a). Improved stall delay model for hawt performance predictions using 3d navier-stokes solver and actuator disk method. *Journal of Applied Fluid Mechanics*, 15, 37–50. https://doi.org/10.47176/jafm.15.01.32651
- Hamlaoui, M. N., Smaili, A., & Fellouah, H. (2021b). New Stall Delay Approach for HAWT Performance Predictions using a CFD Hybrid Method. In *AIAA Scitech 2021 Forum*. https://doi.org/10.2514/6.2021-0951
- Hamlaoui, M. N., Smaili, A., Dobrev, I., Pereira, M., Fellouah, H., & Khelladi, S. (2022). Numerical and experimental investigations of HAWT near wake predictions using Particle Image Velocimetry and Actuator Disk Method. *Energy*, 238, 121660. https://doi.org/https://doi.org/10.1016/j.energy.2021.121660
- International standard IEC/TC 88.61400-11 Ed.2. (2012). Wind turbines Part 11: Acoustic noise measurement techniques. Wind turbines Part 11: Acoustic noise measurement techniques, 2. International Electrotechnical Commission/ Technical Committee.
- International Standard ISO 3744. (2010). Acoustics—Determination of sound power levels and sound energy levels of noise sources using sound pressure—Engineering methods for an essentially free field over a reflecting plane. Acoustics-Determination of sound power levels and sound energy levels of noise sources using sound pressure—Engineering methods for an essentially free field over a reflecting plane. International Organization for Standardization.
- International Standard ISO 9613-2. (1996). Acoustics-Attenuation of sound during propagation outdoors Part 2: General method of calculation. *Acoustics-Attenuation of sound during propagation outdoors Part 2: General method of calculation*. International Organization for Standardization.
- International Standard ISO-1996-1. (2016). Acoustics Description, measurement and assessment of environmental noise Part 1: Basic quantities and assessment procedures. Acoustics Description, measurement and assessment of environmental noise Part 1: Basic quantities and assessment procedures. International Organization for Standardization.
- Khelladi, S. (2024). DGFEM-CAA github repository, https://github.com/skhelladi/DGFEM-CAA/tree/main, accessed: 2025-07-17.
- Khelladi, S., Nogueira, X., Bakir, F., & Colominas, I. (2011). Toward a higher order unsteady finite volume solver based on reproducing kernel methods. *Computer Methods in Applied Mechanics and*

- *Engineering*, 200, 2348–2362. https://doi.org/10.1016/j.cma.2011.04.001
- Kim, D., Lee, G.-S., & Cheong, C. (2015). Inflow broadband noise from an isolated symmetric airfoil interacting with incident turbulence. *Journal of Fluids and Structures*, 55, 428–450. https://doi.org/10.1016/j.jfluidstructs.2015.03.015
- Kwong, W. Y., Zhang, P. Y., Romero, D., Moran, J., Morgenroth, M., & Amon, C. (2012). Wind farm layout optimization considering energy generation and noise propagation. *International Design Engineering Technical Conferences and Computers and Information in Engineering Conference*, 45028, pp. 323–332. https://doi.org/10.1115/DETC2012-71478
- Legendre, C., DeBrye, B., Detandt, Y., Talbot, A., Poulos, A., & Raskin, M. (2018). Broadband Noise Prediction of Stochastic Sources Based on the Linearized Euler Equations. *INTER-NOISE and NOISE-CON Congress and Conference Proceedings*, 258, pp. 3217–3228.
- Lin, M., & Porté-Agel, F. (2022). Large-eddy simulation of a wind-turbine array subjected to active yaw control. *Wind Energy Science*, 7, 2215–2230. https://doi.org/10.5194/wes-7-2215-2022
- Luo, K. H., & Lai, H. (2006). A hybrid LES-acoustic analogy method for computational aeroacoustics. In *Direct and Large-Eddy Simulation VI* (pp. 537–544). Springer.
- Masson, C., Smaïli, A., & Leclerc, C. (2001, October). Aerodynamic analysis of HAWTs operating in unsteady conditions. *Wind Energy*, 4, 1-22. https://doi.org/10.1002/we.43
- Mittal, A. (2010). Optimization of the layout of large wind farms using a genetic algorithm. Master's thesis, Case Western Reserve University.
- Nyborg, C. M., Fischer, A., Réthoré, P.-E., & Feng, J. (2023). Optimization of wind farm operation with a noise constraint. *Wind Energy Science*, 8, 255–276. https://doi.org/10.5194/wes-8-255-2023
- Rahmani, R., Khairuddin, A., Cherati, S. M., & Pesaran, H. M. (2010). A novel method for optimal placing wind turbines in a wind farm using particle swarm optimization (PSO). 2010 Conference Proceedings IPEC, (pp. 134–139).
- Robin, X., & Legendre, C. (2002). Aeroacoustic simulation of multiple wind turbine source interactions. 7th International Conference on Wind Turbine Noise Rotterdam. update, 2002.
- Schepers, J. G., Boorsma, K., Cho, T., Gomez-Iradi, S., Schaffarczyk, P., Jeromin, A., Lutz, T., Meister, K., Stoevesandt, B., Schreck, S., & others. (2012). Final report of IEA task 29, Mexnet (phase 1): analysis of Mexico wind tunnel measurements.
- Shen, W. Z., Mikkelsen, R., Sørensen, J. N., & Bak, C. (2005). Tip loss corrections for wind turbine computations. *Wind Energy: An International*

Journal for Progress and Applications in Wind Power Conversion Technology, 8, 457–475. https://doi.org/10.1002/we.153

Shen, W. Z., Zhu, W. J., Barlas, E., & Li, Y. (2019). Advanced flow and noise simulation method for wind farm assessment in complex terrain. *Renewable Energy*, 143, 1812-1825. https://doi.org/https://doi.org/10.1016/j.renene.2019.05.140

Sorkhabi, S. Y., Romero, D. A., Yan, G. K., Gu, M. D., Moran, J., Morgenroth, M., & Amon, C. H. (2016). The impact of land use constraints in multi-objective energy-noise wind farm layout optimization. *Renewable Energy*, 85, 359–370. https://doi.org/10.1016/j.renene.2015.06.026

Tadamasa, A., & Zangeneh, M. (2011). Numerical prediction of wind turbine noise. *Renewable Energy*, 36, 1902-1912. https://doi.org/https://doi.org/10.1016/j.renene.2010. 11.036

Tingey, E. B., & Ning, A. (2017). Trading off sound pressure level and average power production for wind farm layout optimization. *Renewable*, 114,

APPENDIX A (MESH SENSITIVITY ANALYSIS)

A mesh sensitivity analysis was conducted for a single HAWT in a compressible steady-state simulations at an incoming velocity of $U_0 = 15m/s$. In alignment with the approach of Hamlaoui et al. (2021a), the study assessed the predicted torque values relative to the number of actuator disk points, and evaluated the accuracy of nearwake predictions based on the mesh resolution near the wind turbine. The analysis of the impact of varying actuator point numbers employed a parameter (Q_{shift}) defined in Eq.27 as the shift percentage between the torque achieved with a high number of actuator elements $(Q(N_{270}))$, and the torque values from several incremental counts of actuator elements $(Q(N_i))$. Figure A. 1 indicates that beyond 215 actuator points, further increases yield minimally change in torque value. This suggests that 215 points is a critical threshold for capturing accurate torque without unnecessary computational expense.

$$Q_{shift} = 100 * \frac{Q(N_{270}) - Q(N_i)}{Q(N_{270})}$$
 27

The accuracy of the axial and the radial velocity components was further assessed at a distance of 0.13R both upstream and downstream of the rotor, where R represent the rotor radius. Figures A. 2 and A. 3reveal that the discrepancies in the radial distribution of both velocity components become insignificant with a mesh resolution of D/64, with D is the rotor diameter. Additionally, the axial distribution represented in Fig. A. 4, are consistent with the radial profiles, confirming that the mesh resolution of D/64 effectively captures the flow characteristics across the rotor plane. It should be mentioned that the pronounced increase in radial velocity near the blade tip in the experimental data is primarily

547–555. https://doi.org/10.1016/j.renene.2017.07.057

Wang, Z.-K., Djambazov, G., Lai, C.-H., & Pericleous, K. (2007). Numerical simulation of flow-induced cavity noise in self-sustained oscillations. *Computing and Visualization in Science*, 10, 123–134. https://doi.org/10.1007/s00791-006-0039-4

Wimshurst, A., & Willden, R. H. (2017). Analysis of a tip correction factor for horizontal axis turbines. *Wind Energy*, 20, 1515–1528. https://doi.org/10.1002/we.2106

Yang, T., Chen, X., Zhao, Q., & Zhao, G. (2022). Numerical study on the noise propagation characteristics of rotor in non-uniform downwash flowfield Based on Linearized Euler Equations. *International Journal of Aeroacoustics*, 21, 731– 765. https://doi.org/10.1177/1475472X221136883

Zergane, S., Smaili, A., & Masson, C. (2018). Optimization of wind turbine placement in a wind farm using a new pseudo-random number generation method. *Renewable Energy*, 125, 166–171. https://doi.org/10.1177/1475472X221136883

attributed to the formation and roll-up of intense tip vortices, which induce localized radial flow acceleration. In contrast, the actuator disk method employed in this study imposes a distributed body forces across the rotor disk and does not resolve individual blade geometries or discrete vortex structures. Moreover, the inclusion of TLCF further attenuates the force distribution near the blade tips, resulting in a smoother radial velocity profile. While this modeling approach effectively prevents the overestimates localized flow features, such as the sharp peak in radial velocity seen in the experimental measurements. These findings indicate that a mesh with 215 actuator points and a resolution of D/64 upstream and downstream of the rotor optimally balances accuracy and

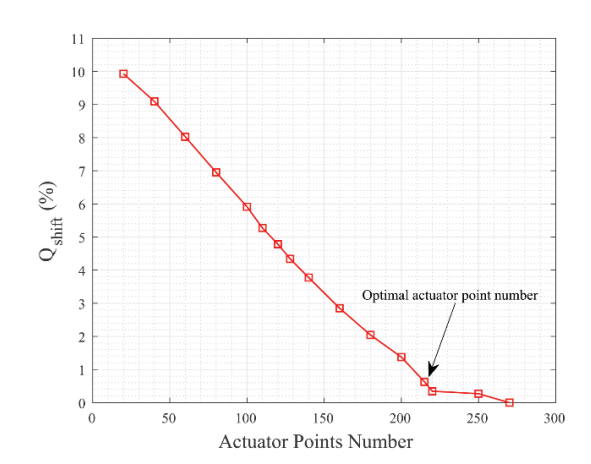


Fig. A. 1 Mesh sensitivity analysis on the optimal grid point number along the rotor blade

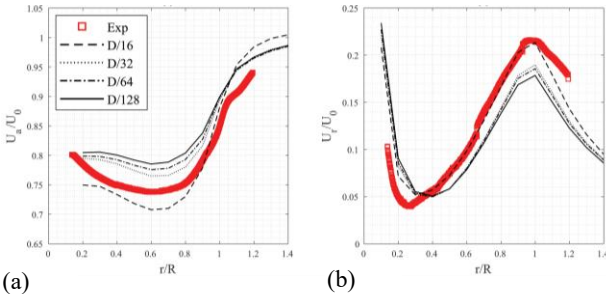


Fig. A. 2 Radial distribution of the (a) axial and (b) radial velocity components measured upstream of the rotor at a distance of 0.13 R

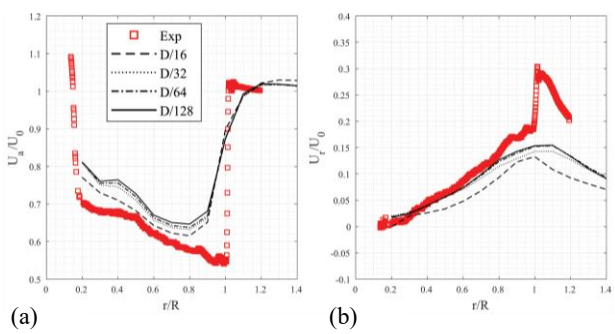


Fig. A. 3 Radial distribution of the (a) axial and (b) radial velocity components measured downstream of the rotor at a distance of 0.13R

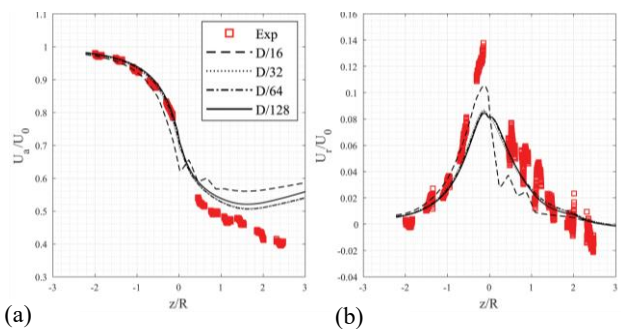


Fig. A. 4 Axial distribution of the (a) axial and (b) radial velocity components obtained at a radial station of r=1.5m

computational efficiency, providing precise velocity distribution with minimal mesh requirements.

Furthermore, a mesh sensitivity study was conducted to ensure accurate resolution of the aeroacoustics analysis. The standard approach for meshing an acoustic model involves selecting element sizes based on the highest frequency considered, typically requiring the wavelength to be 7 to 8 times the element size, significantly increasing the cost of numerical simulations. In this study, Simulations were performed with varying mesh element sizes (2, 1.5, 1, and 0.5 meters) to evaluate the influence of mesh refinement on predicting the OSPL derived downstream the wind turbine at the reference distance, alongside with the ASPL at the same distance. The findings, presented in Table A. 1, indicate that an element size of 1 meter achieves sufficient accuracy while maintaining computational efficiency. The OSPL values exhibit minimal differences between element sizes of 1.5, 1 and 0.5 meters, suggesting that further refinement would not yield significant improvements.

Table A. 1 Impact of mesh refinement on noise levels predictions at the reference distance

	Elements number		249 06	439 24	970 03	4187 17
	Distan ce Eleme nt size [m]		2	1.5	1	0.5
OSPL [dB]	7.25m		80.4	79.9	78.4	83.5
ASPL	7.25m		83.5	83.6	83.5	83.4
[dB]	50	m	79.4	77.9	77.7	76.6

APPENDIX B (VALIDATION OF THE HYBRID PROPOSED APPROACH)

The validation of the proposed hybrid method used in this study was carried out in prior investigation (Amoura et al., 2025), focusing on the well-known NREL Phase VI Horizontal Axis Wind Turbine (HAWT). Simulations covered attached flow, onset of separation, and fully

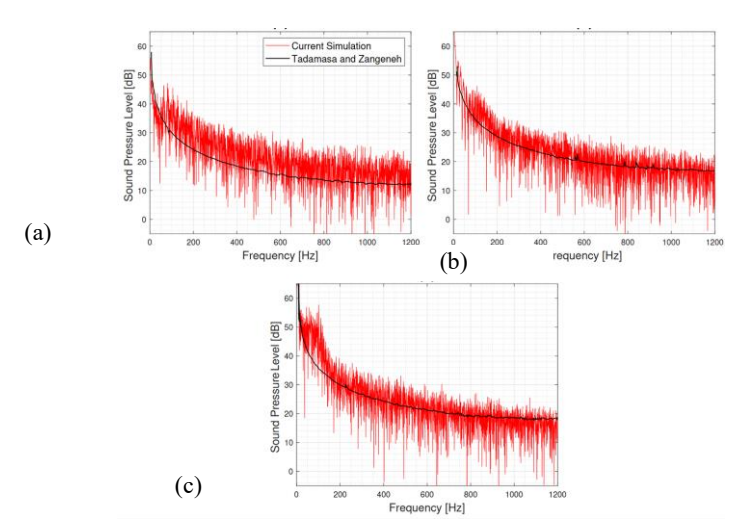


Fig. B. 1 NREL Phase VI SPL Comparison for Various Configurations: (a) U0 = 7m/s, (d) U0 = 9m/s, (c) U0 = 15m/s

stalled conditions, at wind speeds of 7 m/s, 9 m/s, and 15 m/s, respectively. Results were compared to published data from (Tadamasa & Zangeneh, 2011), focusing on Sound Pressure Level (SPL) spectra at a downstream reference point in line with (International standard IEC/TC 88.61400-11 Ed.2, 2012). The comparison

demonstrated strong agreement across all operating regimes. The simulations accurately captured broadband and tonal noise, including dominant blade passing frequency components. Minor discrepancies at high frequencies under fully stalled conditions were likely attributed to challenges in resolving fine-scale turbulence.